In-situ volcanic ash sampling and aerosol-gas analysis based on UAS technologies (AeroVolc)

Simon Thivet[1], Gholamhossein Bagheri[2], Przemyslaw M. Kornatowski[3,4], Allan Fries[1],
Jonathan Lemus[1,5], Riccardo Simionato[1,5], Carolina Díaz-Vecino[1], Eduardo Rossi[1], Taishi Yamada[6],
Simona Scollo[7], and Costanza Bonadonna[1]

[1]Department of Earth Sciences, University of Geneva, Geneva, Switzerland
[2]Max Planck Institute for Dynamics and Self-Organization, Am Faßberg 17, Göttingen 37077, Germany
[3]Institute of Aeronautics and Applied Mechanics, Faculty of Power and Aeronautical Engineering, Warsaw University of
Technology, Warsaw, Poland
[4]Kornatowski Innovation, Ecublens, Switzerland
[5]Department of Computer Science, University of Geneva, Geneva, Switzerland
[6]Research Center for Volcano Hazards Mitigation, Disaster Prevention Research Institute, Kyoto University, Kagoshima,
Japan
[7]Istituto Nazionale di Geofisica e Vulcanologia, Osservatorio Etneo, Piazza Roma 2, 95125 Catania, Italy

Correspondence: Simon Thivet (simonthivet@unige.ch)

Abstract.

Volcanic degassing and explosive eruptions inject significant amounts of gas and ash into the atmosphere, impacting the local environment and atmospheric dynamics from local to global scales. While ground- and satellite-based remote sensing systems are key to describing explosive volcanism and assessing associated hazards, direct *in situ* measurements inside volcanic clouds are not possible with these methods. This study presents an innovative approach using an Unoccupied Aircraft System (UAS) for (i) airborne ash sampling and (ii) measurements of aerosol and gas concentrations (AeroVolc system). Commercial instruments (DJI[TM] Matrice 30 Unoccupied Aerial Vehicle (UAV), Alphasense[TM] N3 Optical Particle Counter OPC, Soarability[TM] Sniffer4D Mini2 multigas hardware) were combined with custom-built ash collectors and particle counters to enable a more detailed analysis of volcanic clouds. Here we showcase the deployment of our UAS on Sakurajima (Japan) and Etna (Italy), two volcanoes known for their frequent explosive eruptions and persistent degassing activity, to demonstrate how this approach enables *in situ*, high-resolution sample and data collection within challenging environments. Results provide grain size distributions (GSDs), information on the occurrence of particle aggregation, as well as solid aerosol (PM_1, $PM_{2.5}$, and PM_{10}) and gas (SO_2 and CO_2) concentrations. Depending on whether the UAS was operated within or below ash- and/or gas-rich clouds, different insights were gained that open up new perspectives for volcanological research. These insights include the composition, concentration, generation, dispersion and sedimentation patterns of volcanic clouds.

1   Introduction

The direct observation of natural processes is a cornerstone of scientific inquiry, providing invaluable insights into process dynamics (e.g., Lenton, 2016; Paredes-Mariño et al., 2022; Singh, 2024). However, this task becomes complex when the pro-

cesses under study occur in remote and/or hazardous environments. This complexity arises from multiple factors, including the

20 inaccessibility of studied locations, the dynamic and often unpredictable nature of the studied processes, as well as the potential risks to researchers and equipment. These challenges necessitate the development and deployment of advanced observational technologies and methodologies, such as remote sensing, autonomous and robust systems, as well as remotely piloted vehicles (cf. Bellingham and Rajan, 2007; Watts et al., 2012; Giordan et al., 2018, for reviews, classifications, and general considerations of the use of remote systems in science). For instance, unoccupied aircraft systems (UASs), which include unoccupied

25 aircraft vehicles (UAVs, sometimes also called drones or remotely piloted aerial systems RPASs) and associated equipment (i.e., embedded and payload instruments) are used for the potential analysis of flood inundation, flood monitoring, and post-flood changes (e.g., Costa et al., 2016; Le Coz et al., 2016; Izumida et al., 2017), for wildfires monitoring (e.g., Martínez-de Dios et al., 2011; Tang and Shao, 2015; Allison et al., 2016), for landslides recognition, monitoring, and hazard assessment (e.g., Giordan et al., 2015; Liu et al., 2015; Lindner et al., 2016), as well as for early impact assessment of earthquakes and

30 building damage assessment (e.g., Boccardo et al., 2015; Fernandez Galarreta et al., 2015; Hirose et al., 2015).

Recent volcanic studies have also made use of UASs to obtain unprecedented access to remote and/or hazardous volcanic environments, improving our understanding of volcano-related processes (cf. Jordan, 2019; Antoine et al., 2020; James et al., 2020, for reviews, classifications, and general considerations of the use of UASs in volcanology). More specifically, UASs are used for imaging, georeferencing, and photogrammetric surveys using visible wavelength, thermal, and multi-spectral cameras

35 (e.g., Zorn et al., 2019; Thivet et al., 2020a; Civico et al., 2021), for geophysical surveys using magnetic and gravity sensors (e.g., Funaki et al., 2014; Gailler et al., 2021; Koyama et al., 2021), and for in-situ measurement and sampling missions using multigas and particle sensors and collectors (e.g., Liu et al., 2019; Schellenberg et al., 2019; Sibaja-Brenes et al., 2023). Employing UASs has been also proven to be an invaluable tool for assessing volcanic hazards, conducting multidisciplinary volcano monitoring, and responding to volcanic crises (e.g., Neal et al., 2019; Gailler et al., 2022; Román et al., 2022).

40 Among the many phenomena associated with volcanic activity, ash (i.e., pyroclastic particles measuring less than 2 mm in diameter) and gas (e.g., water vapor H_2O, sulfur dioxide SO_2, carbon dioxide CO_2) emissions represent significant hazards in most volcanic unrests and eruptions. These emissions usually form plumes (i.e., vertical buoyant columns of ash and gas rising from the volcanic vents) and clouds (i.e, horizontal currents of ash and gas moving in the atmosphere due to density contrasts and/or winds) of various sizes, concentrations, and lifetimes (e.g., Delmelle, 2003; Jenkins et al., 2015; Bonadonna et al., 2021).

45 The intricate interplay between volcanic ash, gas emissions, and the atmosphere represents a complex challenge, necessitating innovative and complementary approaches for comprehensive investigation. Ground-based sampling, analysis of deposits and gas (e.g., Marchetti et al., 2022; Thivet et al., 2022; Pering et al., 2024), as well as ground- and satellite-based remote sensing approaches (e.g., Marzano et al., 2013; Thivet et al., 2021; Guéhenneux and Gouhier, 2024), are crucial to characterize eruptive and degassing processes, but they miss what is dynamically occurring inside volcanic plumes and clouds. In parallel, numerical

50 models have been developed to allow better anticipation and mitigation of the impacts of such natural events (cf. Folch, 2012; Costa et al., 2016; Suzuki et al., 2016, for reviews). However, some local, key parameters and mechanisms occurring at smaller scales (e.g., *in situ* grain size distribution GSD, particle aggregation, settling-driven gravitational instabilities SDGIs, and local

Atmospheric
Measurement
Techniques
Discussions

Open Access

EGU

gas fluctuations) cannot be fully studied with these methods and need to be investigated using dedicated numerical or analog experiments (e.g., Fries et al., 2021; Lemus et al., 2021; Diaz-Vecino et al., 2023).

55   To contribute to the understanding of volcanic clouds, this paper presents an innovative use of an UAS specifically tailored for the in-situ sampling of volcanic ash and measurements of key atmospheric parameters, especially SO_2, CO_2, particulate matter 1, 2.5, and 10 (PM_1, $PM_{2.5}$, and PM_{10}, corresponding to solid aerosol particles with a diameter lower than 1, 2.5, and 10 µm, respectively), as well as pressure (P), temperature (T), and relative humidity (RH) inside, or below these clouds, in a fully controlled manner and with high spatial and temporal resolutions. These key measurements are usually performed at ground

60   level or in manned aircraft far from the sources (e.g., Eliasson et al., 2016; Fries et al., 2023; Pering et al., 2024). Airborne ash sampling has also been tested but without any spatial or temporal control (only using sticky tape on the UAV hull, cf. Mori et al. 2016) or with collectors directly exposed to the airflow of a fixed-wing UAV (which precludes the possibility of ash fallout sampling, cf. Schellenberg et al. 2019). PM measurements (Sasaki et al., 2021) and gas sampling (Shingubara et al., 2021) have also been carried out by UASs but never coupled with controlled particle sampling that could help characterizing

65   the measured sample. The technologies described hereafter are meant to encompass the aspects described above and are meticulously engineered to withstand the harsh conditions encountered in hazardous volcanic environments (i.e., high levels of PM and gas concentrations), as well as unpredictable weather patterns (i.e., sudden changes in P, T, and RH).

To demonstrate the efficacy of this approach, we present results from two campaigns conducted in November 2023 at Sakurajima volcano (Japan) and in July 2024 at Etna volcano (Italy), known for their frequent explosive and degassing activities

70   (Scollo et al., 2014; Poulidis et al., 2018; Iguchi et al., 2022). Through a series of UAV flights both adapted to the environmental conditions and the instruments, we demonstrate the capability of the presented UAS to efficiently perform ash sampling and high-resolution data acquisition in challenging environments. We finally propose several perspectives on using and integrating these UAS technologies to study the processes involved in volcanic plume generation, as well as volcanic cloud composition, concentration, dispersion, and sedimentation.

75   ## 2   Methods

2.1   Unoccupied aircraft vehicle (UAV)

The DJI^{TM} Matrice 30 (Figure 1) was selected as the operated UAV to ensure optimal performance and reliability in challenging volcanic environments based on various considerations. First, its suite of robust features offers excellent performance in volcanic settings. Second, its embedded sensors are useful for flight navigation and object characterization. Third, the associ-

80   ated autonomy, transmission, and maneuverable capacities allow for long and far flights. Finally, its payload versatility allows the simultaneous use of external instruments. All these aspects are described in detail below. Note that a full description of the UAV is available from the manufacturer (https://enterprise.dji.com/matrice-30).

Volcanic environments are notorious for their abrasive nature, especially because airborne volcanic ash poses a significant threat to the integrity of UAS components (Brosch, 2022). Weather conditions, especially relative humidity, the occurrence of rainfall, and wind can also be a limitation for UAV operational capacity (Gao et al., 2021). An important consideration

85

in selecting this UAV is its excellent dust- and water-proof design, reaching the IP55 (IP for ingress protection, the first and second digits are ratings for solids and liquids on a scale from 0 to 6 and from 0 to 9, respectively) international standard IEC 60259 (IEC for international electrotechnical commission). This standard is used to rate the degree of protection or sealing effectiveness in electrical and mechanical enclosures against intrusion of solid particles and liquid droplets, meaning that this

90 UAV is protected against ingress of dust and powerful water jets. The IP55 protection category ensures that UAV internal mechanisms remain shielded from abrasive volcanic ash particles and intense rainfalls, thus mitigating the risk of operational failures and prolonging the lifespan of the UAV (in addition to the anti-collision sensors). Moreover, the UAV can operate between -20 to 50 °C, at a maximum altitude of 7000 m above sea level (asl), and with a maximum recommended wind speed of 12 m s^{-1} (ca. 43 km h^{-1}), therefore accommodating a wide range of environmental conditions.
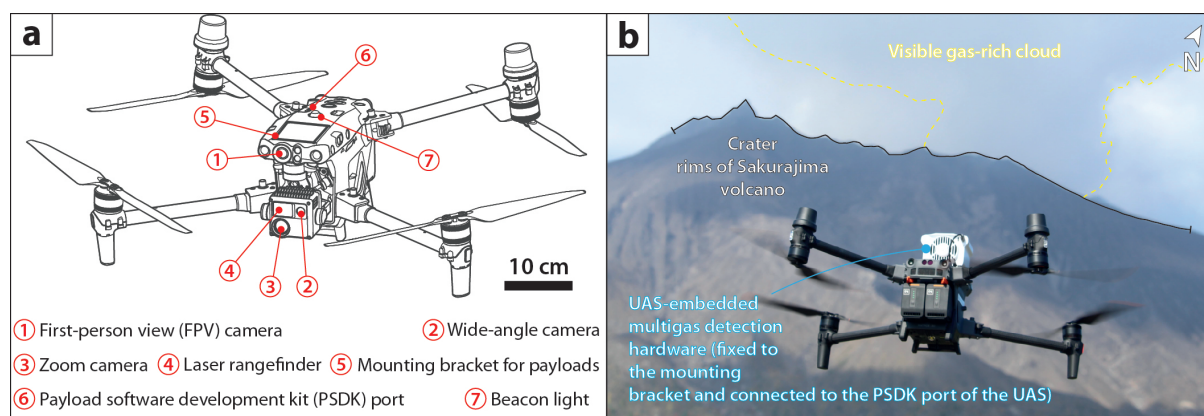
Figure 1. DJI^{TM} Matrice 30 unoccupied aircraft vehicle (UAV). (a) Schematic of the UAV illustrating the main characteristics described in the text. (b) Photo of the UAV in flight (just after takeoff and heading to the visible gas-rich cloud on the morning of the 7th of November 2023) at Sakurajima, carrying the Soarability^{TM} Sniffer4D Mini2 multigas hardware (cf. text for more description).

95 The UAV has an advanced camera system designed to navigate precisely and safely in difficult areas and capture valuable imagery in all directions. It includes a first-person view (FPV) camera used to optimize images in low light conditions, a wide-angle camera for the high-resolution recording of general scenes, and a zoom camera for capturing specific and distant targets (labels 1, 2, and 3 in Figure 1a, respectively). The UAV also features a laser rangefinder (i.e., telemeter, cf. label 4 in Figure 1a) to measure the distance of targeted objects from 3 to 1200 m. When coupled with the global navigation satellite systems

100 (GNSS) of the UAV, specific targets can be accurately positioned in space. Note that an optional thermal camera can also be originally implemented in the UAV (DJI^{TM} Matrice 30T model, not used in this study).

Another key advantage of the UAV is its extended battery life, providing ample autonomy for prolonged missions up to ca. 40 min. Covering extensive areas without frequent battery changes enhances operational efficiency. It maximizes data collection efforts, crucial for comprehensive monitoring and research of dynamic changes in volcanic activity over time. Note that the

105 batteries (DJI^{TM} TB30) can be easily changed to quickly chain the flights. Furthermore, the small size (i.e., 365 x 215 x 195 mm in folded position), lightweight (i.e., 3770 g without payload, maximum recommended takeoff weight of 4069 g), and

Atmospheric
Measurement
Techniques
Discussions

Open Access

EGU

quadcopter (i.e., four rotors) nature of the UAV renders it exceptionally transportable in the field and maneuverable in flight, allowing precise navigation through complex terrain as well as stationary or mobile sampling and measurement missions.

110   The UAV boasts a payload capacity suitable for accommodating external instruments (maximum recommended of 299 g). This capability facilitates the integration of specialized sampling and sensor devices (cf. Figures 1a, 2, and subsections hereafter), enabling real-time sample and data acquisition without compromising flight stability or maneuverability. Payload devices are attached thanks to mounting brackets (label 5 in Figure 1a) and some of them can be directly connected to the payload software development kit (PSDK) port of the UAV (label 6 in Figure 1a) to be supplied in energy and to directly display acquired data in real-time through the UAV remote controller. The UAV Beacon light is also shown (label 7 in Figure

115   1a) as it is used to control some of the payload devices described in the following subsection. Of paramount importance, numerical and experimental studies on quadcopters have consistently shown that turbulence is predominantly generated below each UAV propeller, with only minor turbulence occurring above them. Notably, there is an absence of significant turbulence in the areas between and above the propellers (e.g., Hwang et al., 2015; Ventura Diaz and Yoon, 2018; Carreño Ruiz et al., 2022), which is where payload devices are typically located. This minimal turbulence generation in these regions is crucial for the

120   stable operation of UASs during flight. This feature is particularly advantageous for volcanic ash sampling as well as aerosol and gas analysis, which are thus not impacted during UAV flights.

   Note that the remote controller of the UAV has an integrated screen that provides all information about the UAV, shows videos from all cameras, and allows to control additional payloads. Moreover, it has IP54, which is also crucial for harsh conditions. The remote controller allows long-range operation and telemetry data transmission, even though the UAV can fly

125   autonomously.

2.2   Payload instruments

In the present study, we show four different payload instruments that can be installed on the UAV and used individually. Three instruments were fully developed in-house and dedicated to airborne ash collection (airborne ash collector device A_2C) with additional particle counting (airborne ash collector and counter device A_2C_2) and image recording (airborne ash collector and

130   counter with camera device A_2C_3). Finally, a commercial instrument was acquired (Soarability^{TM} Sniffer4D Mini2 multigas hardware) for atmospheric multigas analysis and particle concentration.

2.2.1   Airborne ash collector (A_2C)

The newly developed A_2C (Figure 2a) is dedicated to airborne volcanic ash sampling at controlled altitudes and distances from the emission sources (i.e., active volcanic vents). It is made of robust metallic, and 3D-printed plastic pieces, as well as low-

135   priced commercially available devices and consumables, potentially facilitating their widespread use in the study of airborne volcanic ash. Electrical components are sealed with rubber or silicon to avoid any potential abrasion or corrosion. The total weight of the device is 170 g, thus suitable for the UAV maximum recommended takeoff weight. The device can be fixed to the UAV thanks to an attachment support for the UAV mounting bracket (label 1 in Figure 2). It is independently powered by a small rechargeable lithium-ion battery of 7.4 V and 400 mAh (label 2 in Figure 2) capable of powering the entire device
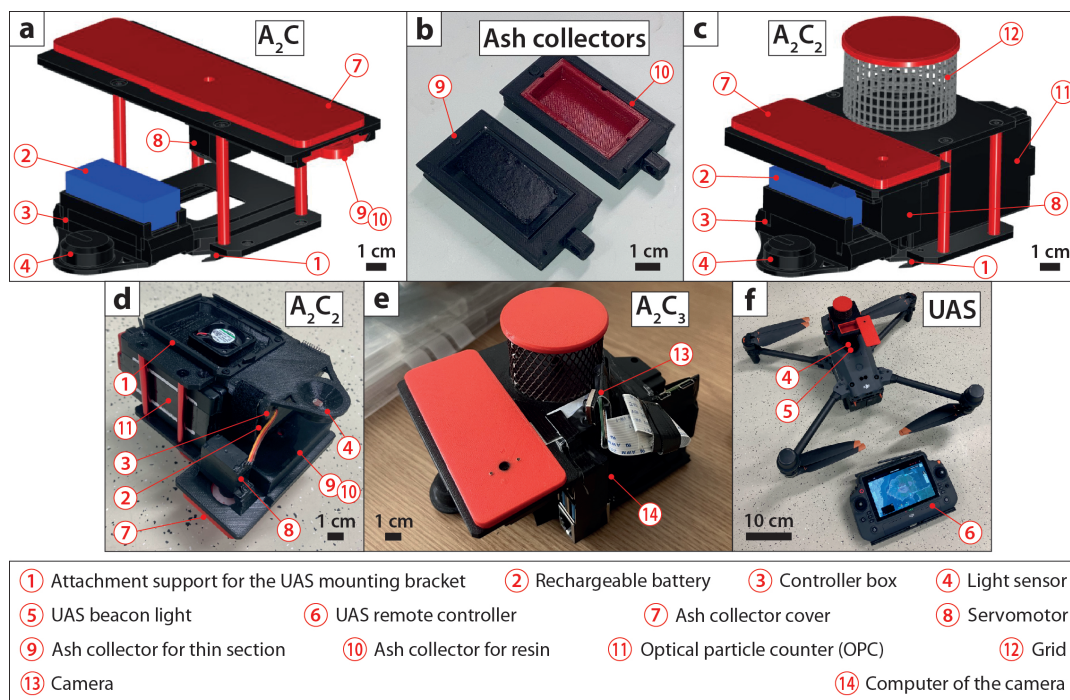
Figure 2. Payload instrument developed in-house. (a) Schematic (isometric view) of the airborne ash collector device (A_2C) dedicated to ash sampling only (it has two ash collector slots). (b) Photo of the two types of ash collectors. The bottom collector hosts a glassy thin section with conductive carbon adhesive tape, while the top collector is designed to host ultraviolet (UV) resin. (c) Schematic (isometric view) of the airborne ash collector and counter device (A_2C_2) dedicated to ash sampling (one ash collector slot) and simultaneous fine ash counting. Counting is performed by an integrated Alphasense^{TM} optical particle counter (OPC) N3. (d) Photo (view from the bottom) of the A_2C_2 where the OPC outlet fan and the light sensor are visible. (e) Photo of the airborne ash collector and counter with camera device (A_2C_3) dedicated to ash sampling, counting, and image recording. Images are recorded by a Raspberry Pi Camera module 3 connected to a Raspberry Pi 4 Model B single board computer. (f) Photo of the A_2C_2 attached to the unoccupied aircraft vehicle (UAV) ready to fly. Note that the ash collector cover is open as the beacon light of the UAV is off. See the text for a more detailed explanation.

140 for ca. 5 h, which is largely enough when compared to the UAV autonomy. The battery is directly linked to the electronic controller box (label 3 in Figure 2). A light sensor (label 4 in Figure 2) is designed to be positioned directly above the UAV beacon light (label 5 in Figure 2) that can be switched on and off directly with the UAV remote controller (label 6 in Figure 2). The electronic controller is programmed to close the ash collector cover (label 7 in Figure 2) when the beacon light is on and to open the cover when the beacon light is off, thanks to a servomotor (label 8 in Figure 2) that can rotate the ash collector

145 cover by 90°. Hence, the UAS operator has full control over when and where to confidently perform volcanic ash sampling, which is the leading innovative point achieved by this device. Note that contrary to uncontrolled collection methods (Mori et al., 2016) and to collectors directly exposed to a fixed-wing UAV airflow (Schellenberg et al., 2019), the A_2C is designed to collect particles that are settling vertically (i.e, ash fallouts). When the ash collector cover is open, samples can be collected in

6

two types of ash collector (Figure 2b). One collector is designed to hold conductive carbon tape stuck on a glassy thin section

150 of standard dimensions of 48 x 28 mm (label 9 in Figure 2). This technique was previously performed in various studies at ground level (e.g., Bonadonna et al., 2011; Bagheri et al., 2016; Gabellini et al., 2022). The second collector is designed with an additional rubber tank of inner dimensions of 43 x 23 mm (label 10 in Figure 2) that can accommodate ultraviolet (UV) resin, which can better conserve the structure of potential particle aggregates during sampling compared to the use of carbon tape (Gabellini et al., 2024) and which can be immediately solidified after the UAV landing using a UV lamp. Note that the

155 A_2C displays two sampling slots, hence it can perform the two sampling methods simultaneously. This can be useful for further and different laboratory analyses (e.g., Gurioli et al., 2022; Ross et al., 2022; Gabellini et al., 2024).

2.2.2 Airborne ash collector and counter (A_2C_2)

To better interpret the collected airborne ash samples, we also used an optical particle counter (OPC) for *in-situ* and real-time measurement of fine GSDs (i.e., below 40 µm) and PM_1, $PM_{2.5}$, and PM_{10} concentrations (Bonadonna et al., 2012). Therefore,

160 the A_2C_2 was developed (Figures 2c and d). It shares the same characteristics as the A_2C, but it has only one sampling slot, which allows more space to integrate an Alphasense[TM] N3 OPC (label 11 in Figure 2). Note that the total weight of the device is 250 g, which is also suitable for the UAV maximum recommended takeoff weight.

This OPC is recognized by the international organization for standardization (ISO) 9001:2015 certification. This device uses an embedded laser diode (658 nm, class 1 laser product as the laser source is inaccessible). Similarly to conventional

165 OPCs, it measures the light scattered by solid particles carried in a sample air stream through a laser beam. Raw data are used to determine particle sizes, which are related to the intensity of light scattered via a calibration based on the Mie scattering theory (Flagan and Seinfeld, 2012). PM_1, $PM_{2.5}$, and PM_{10} concentrations are directly calculated from the raw particle count spectra assuming a standard particle density (which can be changed as volcanic particles usually span a density range between 2490 and 2980 kg m^{-3} depending on their size and composition, cf. Vogel et al. 2017) and refractive index (equal to 1.5,

170 which is coherent with values of fine volcanic particles, also cf. Vogel et al. 2017). The detection range is from 0.3 to 40 µm (spherical equivalent size) and data (acquired every 1.398 s) is stored in the integrated memory of the OPC. This device is factory-calibrated using particles of known diameter and refractive index. Tests confirmed that the way the A_2C_2 is displayed on the UAV does not restrict its airflow (from its intake pointed upwards, to its outtake pointed downwards). However, because fan speed can vary, the sample flow rate through the OPC may also change (0.21 L min^{-1} on average). Such variations are

175 monitored and corrected dynamically by the OPC so that the particle concentrations and derived PM values are unaffected by moderate flow variations. The OPC has onboard T and RH sensors. Note that a full description of the OPC is available from the manufacturer (https://www.alphasense.com/products?keyword=opc-n3). Also note that as the airflow intake of the OPC is pointed upwards, a particle umbrella and grid (mesh of 2 x 4 mm), which is not interfering with particle flow, is displayed around the air intake to avoid large objects from entering the unit (label 12 in Figure 2).

2.2.3 Airborne ash collector and counter with camera (A_2C_3)

In a third step, the A_2C_3 was further developed by adding a miniaturized camera to the A_2C_2 (Figure 2e). The camera is facing the ash collector to image sequences of falling particles. The objective is to monitor particle size and settling velocity, as well as to document if particles bounce or break following impact on the ash collector. Images are particularly useful for distinguishing between the different types of ash aggregates (Brown et al., 2012; Bagheri et al., 2016; Diaz-Vecino et al., 2022), as images allow us to visualize how aggregates eventually break upon impact on the ash collector. Note that the total weight of the device seats right at the maximum recommended payload UAV capacity (299 g).

The camera is a Raspberry Pi Camera Module 3, which is small ($25 \times 24 \times 11.5$ mm), lightweight (4 g), low-cost, versatile, and adaptable to a wide range of usages, including volcanology (Wilkes et al., 2017; Andò et al., 2021; Del Rosso et al., 2021). Here, the camera (label 13 in Figure 2) is fixed on the side of the grid and connected to a Raspberry Pi 4 Model B single board computer (label 14 in Figure 2), which is placed on the side of the structure. The computer is powered through the PSDK port of the UAV (label 6 in Figure 1a) and set up to record images automatically on startup. The image resolution is set at 1200×600 pixels, allowing to record videos at a frame rate of ca. 100 fps. The depth of field is fixed at ca. 8 cm in which the spatial resolution is 33 μm per pixel. Videos are saved in the internal memory of the computer. Note that full descriptions of the camera and associated computer are available from the manufacturer (https://www.raspberrypi.com/documentation/accessories/camera.html and https://www.raspberrypi.com/products/raspberry-pi-4-model-b/specifications/).

2.2.4 Multigas detector

In the scope of measuring complementary key atmospheric parameters, a commercial multigas detector developed by Soarability[TM] which is specifically designed for the DJI[TM] Matrice 30 UAV, has been acquired (Figure 1b). This multigas device is called Sniffer4D Mini2 and can obtain up to 9 aerosols and gas concentrations at one time. It is the miniaturized version of the multigas detectors presented in Godfrey et al. (2023). We specifically choose the detection of SO_2, CO_2, PM_1, $PM_{2.5}$, and PM_{10} concentrations to focus on the study of volcanic gases and aerosols (the device also records P, T, and RH). Note that our device version weighs 269 g, which is suitable for the UAV maximum recommended takeoff weight.

This multigas detector is directly connected to the PSDK port of the UAV (Figure 1), which delivers enough energy to power the device and allows real-time data transmission to the UAV remote controller (label 6 in Figure 2). The device's built-in cellular connectivity also enables secure real-time data transmission with unlimited range, which eases the 3D visualization in real-time of gas concentration distributions and adapts UAV flight navigation according to the scientific objectives. Data (acquired every 1 s) is also saved in the device's internal memory. The active air intake fan on the back of the device allows the evacuation of sampled air, the sample flow rate being ca. 10 L min^{-1}. The filter on the front side can filter floating and coarse objects in the air. Note that a full description of the multigas device is available from the manufacturer (https://www.soarability.com/sniffer4d-uav-multi-gas-sensing). All device's modules are calibrated and certified (calibration is recommended every year, using calibration gas chambers).

Atmospheric
Measurement
Techniques
Discussions

Similarly to OPCs, the PM sensing module is based on laser scattering, with a particle counting effectiveness of 50 % at 0.3 μm, rapidly reaching 98 % above 0.5 μm. It can measure particle concentration between 1 and 1000 μg m^{-3} with a maximum measurement deviation of $\pm$ 2 %. The module has an on-chip proprietary humidity correction algorithm, enabling better data quality in a wide humidity range (from 0 to 95 %).

The detection method of the wide-range CO_2 sensing module is based on non-dispersive infrared (NDIR), as commonly encountered for CO_2 sensors (e.g., Rüdiger et al., 2017; Liu et al., 2020; Pering et al., 2024). It can measure CO_2 concentration between 0.01 % (100 ppm) and 5 vol% with a maximum measurement deviation of $\pm$ 2 %. The module has on-chip proprietary environmental and individual difference compensation algorithms, enabling better data quality in wide temperature (from -20 to 50 °C) and relative humidity (from 0 to 95 %) ranges.

Finally, the detection method of the wide-range SO_2 sensing module is based on electrochemistry, as commonly encountered for SO_2 sensors (e.g., Rüdiger et al., 2017; Liu et al., 2020; Pering et al., 2024). It can measure SO_2 concentration between 0.000075 % (750 ppb) and 0.01 % with a maximum measurement deviation of $\pm$ 4 %. The module has on-chip proprietary environmental and individual difference compensation algorithms, enabling better data quality in wide temperature (from -20 to 50 °C) and humidity ranges (15 to 90%).

Note that the overall response time of the PM, CO_2, and SO_2 modules are below 10, 30, and 40 s. All recorded data (P, T, RH, as well as PM, CO_2, and SO_2 concentrations) is automatically synchronized to enable a comparison of these parameters.

2.3 Field strategy and data processing

The aforementioned instruments were deployed at Sakurajima volcano (Figure 3) in November 2023 and Etna volcano (Figure 4) in July 2024. In particular, the A_2C, A_2C_2 and multigas detector were used at Sakurajima, while the A_2C_3 was only tested at Etna.

Sakurajima volcano is situated in the northern part of Kagoshima Bay (Kyūshū, the most southerly of the four largest islands of Japan) (Figure 3a). Since 1955, frequent volcanic activity has been observed either in Minamidake (vent A and B) or in Showa craters. This activity alternates between degassing periods and frequent Vulcanian explosions, both potentially producing ash- and/or gas-rich volcanic plumes and clouds of various intensities and features (e.g., Poulidis et al., 2018; Freret-Lorgeril et al., 2022; Takishita et al., 2024) (Figure 3b). Despite the establishment of a 2 km prohibited zone around the active craters (for a current alert level of 3/5, representative of frequent Vulcanian eruptions), a main road goes around the volcano (which forms a peninsula). This arrangement allowed us to position ourselves directly near/below volcanic clouds depending on the winds and to fly the UAS over the restricted area if needed (Figure 3c).

Etna volcano is situated in the eastern part of Sicily island, in southern Italy (Figure 4a). Volcanic activity, characterized by degassing and Strombolian explosions, as well as intense lava fountains (also named paroxysmal episodes) during paroxysmal eruptions, are usually observed in Bocca Nuova, Voragine (both forming the central craters), north-east, or south-east craters (Figure 4b). Since 2010, Etna has often experienced paroxysmal eruptions generating ash plumes (e.g., Calvari et al., 2018; Marchetti et al., 2022; Scollo et al., 2019). Depending on the wind, areas subject to fallout are mainly affecting the southeast sector of the volcano (Scollo et al., 2013), which is accessible by several roads (Figure 4c).
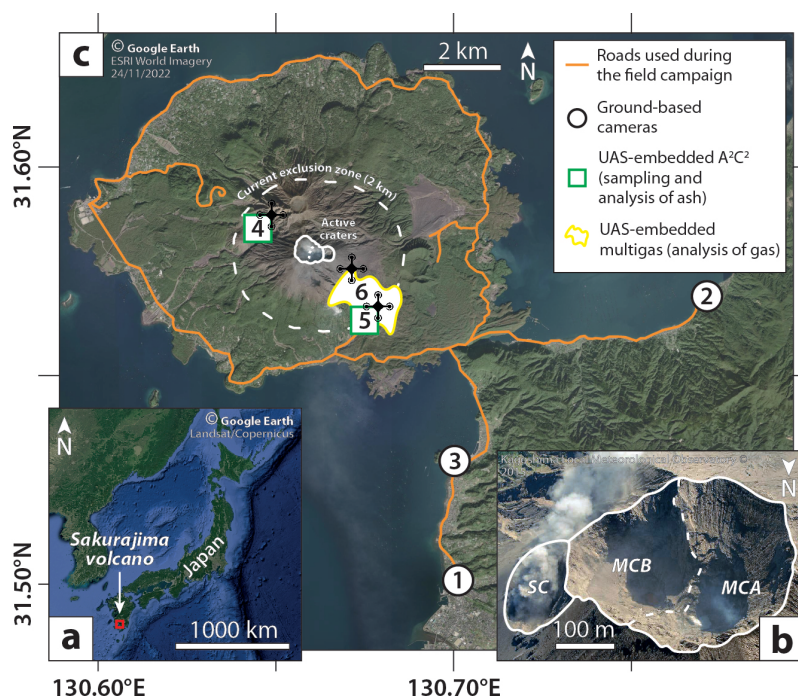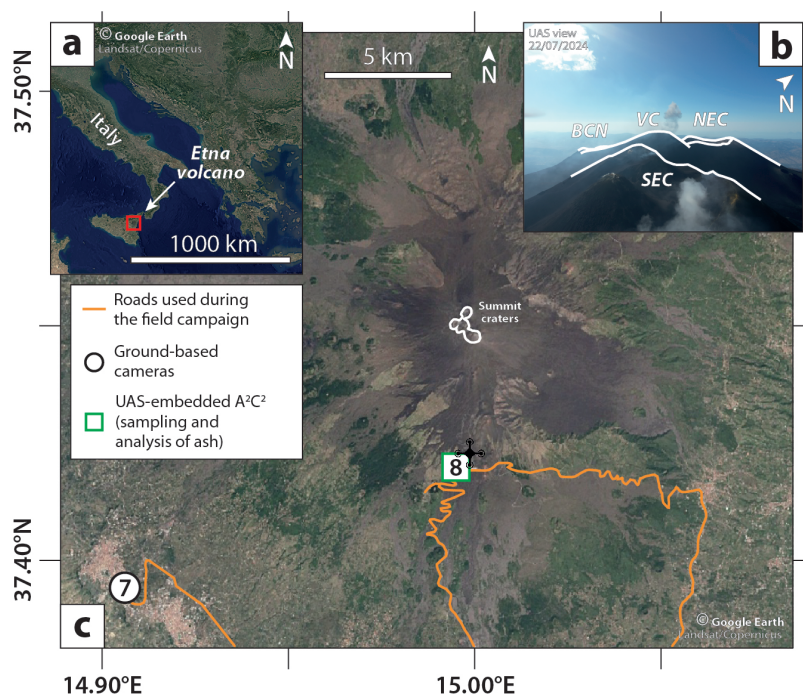
Figure 3. Localisation and general features of Sakurajima volcano. (a) Localisation of Sakurajima at a global scale. (b) Aerial photo of the active craters of Sakurajima. MCA: Minamidake crater vent A; MCB: Minamidake crater vent B; SC: Showa crater. (c) Map of Sakurajima edifice. White lines delimit the summit craters shown in (b). The dashed white circle represents the current exclusion zone (for a current alert level of 3/5, representative of frequent Vulcanian eruptions) delimited 2 km around the active craters.

Note that UAV flights were conducted respecting local rules (e.g., UAV registered to the Swiss, European, and Japanese authorities, no flying over infrastructures and people) with a second operator in charge of securing take-off and landing areas as well as of visually following the UAV as much as possible. Note that UAV flights were restricted to a maximum of 500 and 1500 m above takeoff points at Sakurajima and Etna, respectively.

250   During the field campaigns, ground-based cameras were set up almost perpendicularly to the main dispersal axis of the occurring volcanic clouds to have complementary imaging. Volcanic plumes elevations were inferred following the procedure described in Simionato et al. (2022), also applying a correction to account for the effect of wind detailed in Snee et al. (2023). The wind direction was retrieved from the ERA5 hourly data on pressure levels (Hersbach et al., 2023). This is an important step to locate the UAV's altitude compared to the cloud's altitude.

255   Note that for the OPC measurements, an average PM density of 2500 and 2800 kg m^{-3} has been considered for Sakurajima and Etna, respectively, according to the magma composition of each volcano (Bagheri et al., 2016; Ferlito et al., 2017). OPC raw data (i.e., particle counts) are then converted into mass, considering that all measured particles are spherical.

Ash samples were analyzed in the laboratory with a Keyence^{TM} VHX-7000 optical microscope, which enabled the acquisition of multi-focused (z-stacking technique) high-definition images, at different magnifications (from x100 to x1000), allowing

Figure 4. Localisation and general features of Etna volcano. (a) Localisation of Etna at a global scale. (b) Aerial picture of the active vents of Etna. VC: Voragine crater; NEC: North-east crater; SEC: South-east craters. Note that the Bocca Nuova crater (BNC) seats just behind and at the Base of the Voragine crater in this photo. (c) Map of Etna edifice. White lines delimit the summit craters shown in (b).

260 the reconstruction of the samples GSDs after image binarization. Particle counts are also converted into mass considering spherical particles. Note that a full description of the microscope and associated software is available from the manufacturer (https://www.keyence.com/products/microscope/digital-microscope/vhx-7000/).

3   Results

Three volcanic events at Sakurajima and one event at Etna have been used as case studies. They are representative of different

265 types of volcanic activity (Figure 5), for which UAS sampling and measurements were performed for different objectives scopes. Note the UAV was always live-controlled to be able to adapt in real time the flights, sampling and measurements depending on the volcanic and atmospheric conditions.

The first case study is an explosive event that started at Sakurajima on the 10th of November 2023 at 11:17:25 am (all times provided in this study are local times, format being hh:mm:ss am/pm), from Minamidake crater (acquired data cannot permit to

270 distinguish between vent A or vent B, cf. Figure 5a). It produced a buoyancy-driven ash-loaded plume of relatively low altitude (maximum of ca. 1250 m asl), which was dispersed into two wind-advected clouds associated with two wind directions present at different elevations. The main cloud was dispersed toward the northwest by a downslope wind, which is often occurring at

Sakurajima (Poulidis et al., 2017). This brought the cloud down to ca. 550 m asl (cf. supplementary material, File S1, for the altitude parameterization). This relatively low altitude allowed a direct in-situ UAV flight into the cloud (cf. label 4 in Figure 275 5a) using the A_2C_2 device, as the UAV takeoff point was 408 m asl for this location (at the old observatory near the Yunohira observation deck, with a maximum UAV flight altitude of 908 m asl).

The second case study is an explosive event at Sakurajima that started on the 11th of November 2023 at 02:28:47 pm (Figure 5b), also from Minamidake crater (vent A or vent B). Similarly to the first case study, it produced a buoyancy-driven ash-loaded plume of relatively low altitude (maximum of ca. 1400 m asl). However, the associated ash-loaded cloud dispersed ash towards 280 the southwest and progressively increased in altitude. For instance, the cloud base and top were at ca. 1700 and 2550 m asl, respectively, at 2 km away from the source, where airborne sampling was performed (cf. supplementary material, File S1, for the altitude parameterization). Contrary to the first case study, UAV flight was only possible below the cloud (cf. label 5 in Fig. 5b), as the UAV takeoff point was 85 m asl for this location (at the Arimura lava observation deck, with a maximum flight altitude of 585 m asl), hence scoping the sedimentation of particles associated to the cloud, using the A_2C_2 device.

285 The third case study is a paroxysmal eruption that occurred at Etna on the morning of the 23rd of July 2024 (Figure 5c). Sustained lava fountains were observed from the Voragine crater between ca. 5 am and 10 am. This activity generated a buoyancy-driven ash-loaded plume at an average altitude of 7000 m asl, which derived towards the south because of the wind (cf. supplementary material, File S1, for the altitude parameterization). Thus, the UAV flight was only possible below the cloud (cf. label 8 in Figure 5c), UAV takeoff point being at 1883 m asl for this location (near the Sapienza refuge, with a maximum 290 flight altitude of 2383 m), hence scoping the sedimentation of particles associated to the cloud, using the A_2C_3 device, at 6 km from the vent.

The fourth and last case study is a continuous degassing at Sakurajima, that occurred during the afternoon of the 19th of November 2023, without any explosive event (Figure 5d). This active degassing produced a gas-rich cloud from the Minami-dake crater (vent A or B) that was dispersed to the southwest. Most importantly, this cloud was dispersed from low (ca. 500 m 295 asl) to medium (ca. 2000 m asl) altitudes (cf. supplementary material, File S1, for the altitude parameterization), which allowed to scope the base of this gas-rich cloud using the multigas detector, as the UAV takeoff point was 85 m asl for this location (at the Arimura lava observation deck, with a maximum flight altitude of 585 m asl).

3.1 First case study: ash sampling and analysis with the A_2C_2 device inside the ash-loaded cloud on the 10th of November 2023

300 The first case study is described based on a 9.7 min-long UAV flight, along the trajectory shown in Figure 6a (cf. also supplementary material, File S2, for the UAV flight report). The OPC was active during the whole UAV flight (Figure 6b), but sampling was only performed during 2 min at the closest position of the eruptive source and in a stationary position (cf. label 4 in Figure 6).

Grain size data acquired by the OPC (cf. supplementary material, File S3, for raw data) shows steady baselines both at the 305 beginning and the end of the measurement (i.e., before 11:25:30 am and after 11:29:30 am). The baseline at the beginning is characterized by the slight occurrence of $PM_{2.5}$ with a scarcer occurrence of particles up to 8 μm. As a result, PM_1, $PM_{2.5}$, and
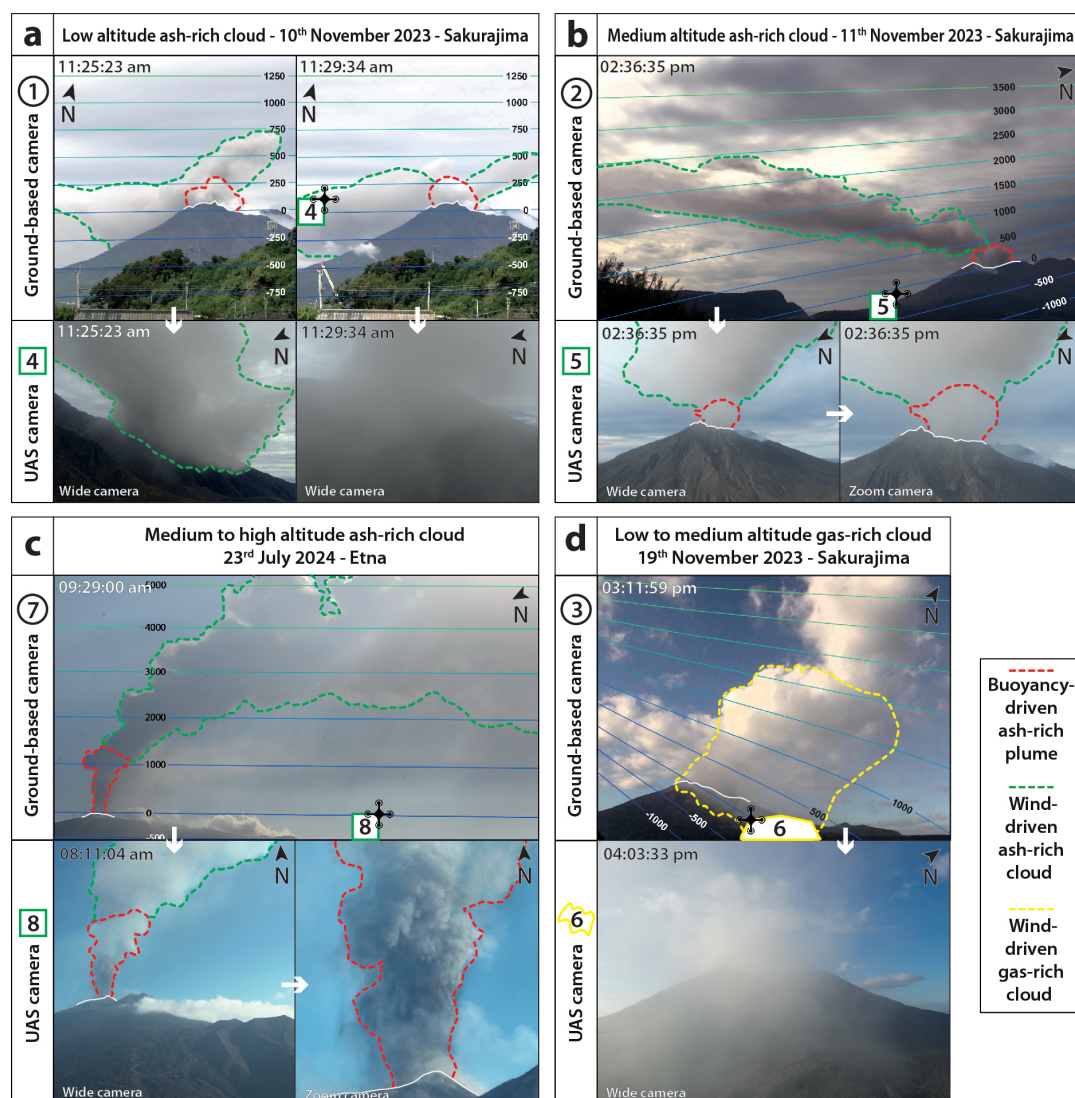
Figure 5. Characterization of the events shown in this study. Labeled sites correspond those shown in Figures 3c ans 4c. All times provided in this study (time format being hh:mm:ss am/pm) are local times. Ground-based photos show equal elevation (m) isolines for each wind-corrected cloud plane (crater rim altitude in the cloud plane is defined at 0 m). (a) Explosive event that started at Sakurajima in the morning of the 10th of November 2023. (b) Explosive event that started at Sakurajima in the afternoon of the 11th of November 2023. (c) Paroxysmal eruption that started at Etna in the morning of the 23rd of July 2024. (d) Continuous degassing that occurred at Sakurajima in the afternoon of the 19th of November 2023.

PM$_{10}$ concentrations are typically lower than 5, 10, and 40 μg m^{-3}, respectively. The baseline at the end is characterized by slightly higher levels of PM concentrations (i.e., maximum of 10, 40, and 100 μg m^{-3} for PM$_1$, PM$_{2.5}$, and PM$_{10}$, respectively) with a scarcer occurrence of particles up to 16 μm.

310   The ash-loaded cloud is identified between 11:25:30 am and 11:29:30 am, as OPC data is characterized by a sudden increase

of particle concentration up to 16 μm, with the scarce occurrence of particles up to 22 μm. As a result, maximum PM_1, $PM_{2.5}$

and PM_{10} concentrations measured in the cloud are 100, 3000, and 80000 μg m^{-3}, respectively. This corresponds to an OPC

grain size mode between 4 and 16 μm (cf. supplementary material, File S3, for histograms), without any significant amount

of particles below and above this range (i.e., good grain size sorting within the OPC measurement range). Also, note that a

315   significant and unlikely lack of PM_1 and $PM_{2.5}$ characterizes two narrow areas in the cloud.
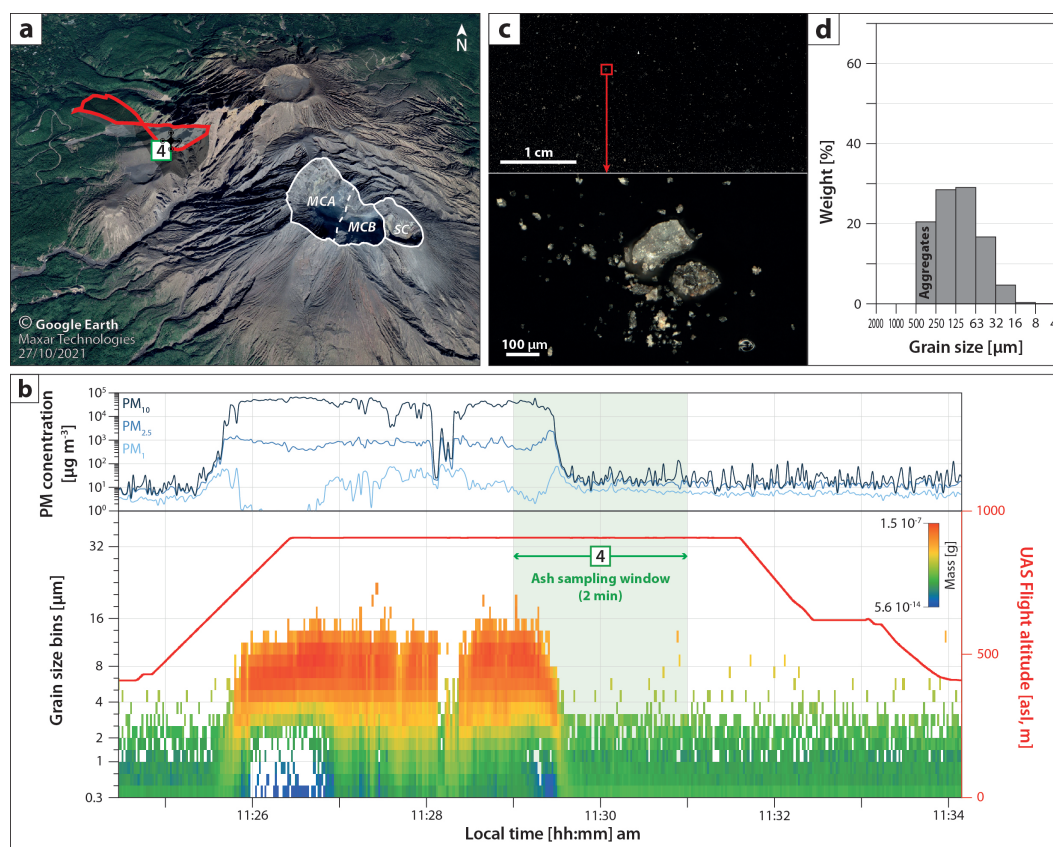
Figure 6. Results obtained by the A_2C_2 device on the 10th of November 2023 explosive event at Sakurajima. (a) UAV flight path (red line) during which the optical particle counter (OPC) analysis was performed. The green square labeled 4 corresponds to the site shown in Figures 3c and 5a, and represents the ash sampling location and duration (also shown in b). White lines delimit the active craters shown in Figure 3b (MCA: Minamidake crater vent A; MCB: Minamidake crater vent B; SC: Showa crater). (b) Particulate matter (PM) concentrations and grain size spectrogram from the optical particle counter (OPC) data. (c) Optical microscopy images of the collected sample at different scales. (d) Grain Size Distribution (GDS) inferred from image analysis of the collected sample.

The ash collector was opened between 11:29 am and 11:31 am, allowing the carbon tape to collect particles from the ash-loaded cloud during ca. 30 s (Figure 6b). Particle distribution on the tape is not homogeneous (most of the particles being

collected on the lower left half of the tape, cf. also Figure 6c and supplementary material, Files S4 and S5, for more detailed images and particle counting). Above the OPC measurement range, the GSD reconstructed from the image analysis of the

320 collected sample (Figure 6d) shows a relatively wide and unimodal distribution, with a mode between 63 and 125 μm. Note that particles above 250 μm should not be considered as single particles but as ash aggregates (all types of particle clusters, PCs, following the Brown et al. 2012 and Bagheri et al. 2016 nomenclatures, are observed, cf. also Figure 6c).

3.2 Second case study: ash sampling and analysis with the A_2C_2 device below the ash-loaded cloud on the 11th of November 2023
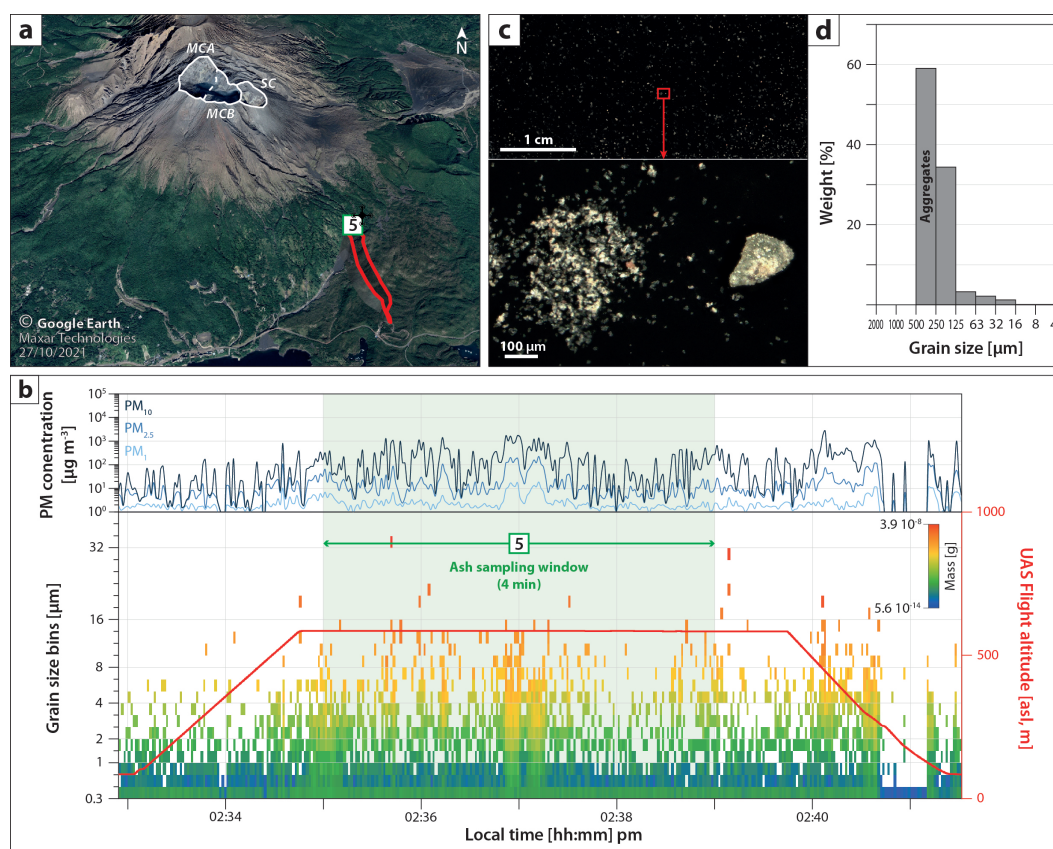
Figure 7. Results obtained by the A_2C_2 device for the 11th of November 2023 explosive event at Sakurajima. (a) UAV flight path (red line) during which the optical particle counter (OPC) analysis was performed. The green square labeled 5 corresponds to the site shown in Figures 3c and 5b, and represents the ash sampling location and duration (also shown in b). White lines delimit the active craters shown in Figure 3b (MCA: Minamidake crater vent A; MCB: Minamidake crater vent B; SC: Showa crater). (b) Particulate matter (PM) concentrations and grain size spectrogram from the optical particle counter (OPC) data. (c) Optical microscopy images of the collected sample at different scales. (d) Grain Size Distribution (GDS) inferred from image analysis of the collected sample.

15

Atmospheric
Measurement
Techniques
Discussions

Open Access

EGU

325   The second case study is described based on a 8.6 min-long UAV flight, along the trajectory shown in Figure 7a (cf. also supplementary material, File S2, for the UAV flight report). The OPC was active during the whole UAV flight (Figure 7b), but A_2C_2 sampling was performed during 5 min at the closest position of the eruptive source and in a stationary position (cf. label 5 in Figure 7).

Grain size data acquired by the OPC (cf. supplementary material, File S3, for raw data) show different patterns compared
330   to those characterizing the first case study. The whole UAV flight outlined an unsteady baseline, characterized by the slight occurrence of particles up to 8 μm, resulting in low PM concentrations with similar values to the beginning baseline of the first case study. However, this baseline is intersected by numerous and brief (i.e., 2 to 20 s) peaks of particles from 0.3 to 32 μm, with a systematic mode between 8 and 16 μm (cf. supplementary material, File S3, for histograms), resulting in spontaneous increase of PM concentrations (i.e., up to 20, 300, and 3000 μg m^{-3} for PM_1, $PM_{2.5}$, and PM_{10}, respectively).

335   The ash collector was opened between 02:35 pm and 02:39 pm, allowing the carbon tape displayed on a thin section to collect particles from the sedimentation of the ash-loaded cloud during 4 min (Figure 7b). Contrary to the first case study, particle distribution on the tape is homogeneous (Figure 7c, cf. also supplementary material, Files S4 and S5, for more detailed images and particle counting). Above the OPC measurement range, the GSD reconstructed from the image analysis of the collected sample (Figure 7d) shows an unimodal and asymmetric distribution, skewed towards relatively coarse sizes, with a
340   mode between 250 and 500 μm. Interestingly, particle aggregation (mostly represented in the 125 to 500 μm range) is much more developed than in the first case study (all types of PCs are observed).

3.3   Third case study: ash sampling and analysis with the A_2C_3 device below the ash-loaded cloud on the 23rd of July 2024

The third case study is described based on a 21.7 min-long UAV flight, along the trajectory shown in Figure 8a (cf. also
345   supplementary material, File S2, for the UAV flight report). The OPC was active during the whole UAV flight (Figure 8b), but A_2C_3 sampling was performed during 7 min above the UAV takeoff position and in a stationary position (cf. label 8 in Figure 8).

Grain size data acquired by the OPC (cf. supplementary material, File S3, for raw data) shows a steady baseline during the whole flight, characterized by the systematic absence of particles above 10 μm and low particle mass below this threshold,
350   resulting in low PM concentrations with similar values as the beginning baseline of the first case study.

The ash collector was opened between 08:10 am and 08:17 am, allowing the carbon tape displayed on a thin section to collect particles from the sedimentation of the ash-loaded cloud for 7 min (Figure 8b). Particle distribution on the tape is homogeneous (Figure 8c, cf. also supplementary material, Files S4 and S5, for more detailed images and particle counting). The GSD reconstructed from the image analysis of the collected sample (Figure 8d) shows an unimodal and narrow distribution,
355   with a mode between 500 and 1000 μm. Also note that ash aggregation is not observed.

The image sequence captured by the camera installed on the A_2C_3 allows to discriminate between particles that are directly falling and sticking in the ash collector (linear trajectories) from particles that are first rebounding on the UAS before being collected (parabolic trajectories). Particle size and falling velocity are estimated for a single particle that has been clearly
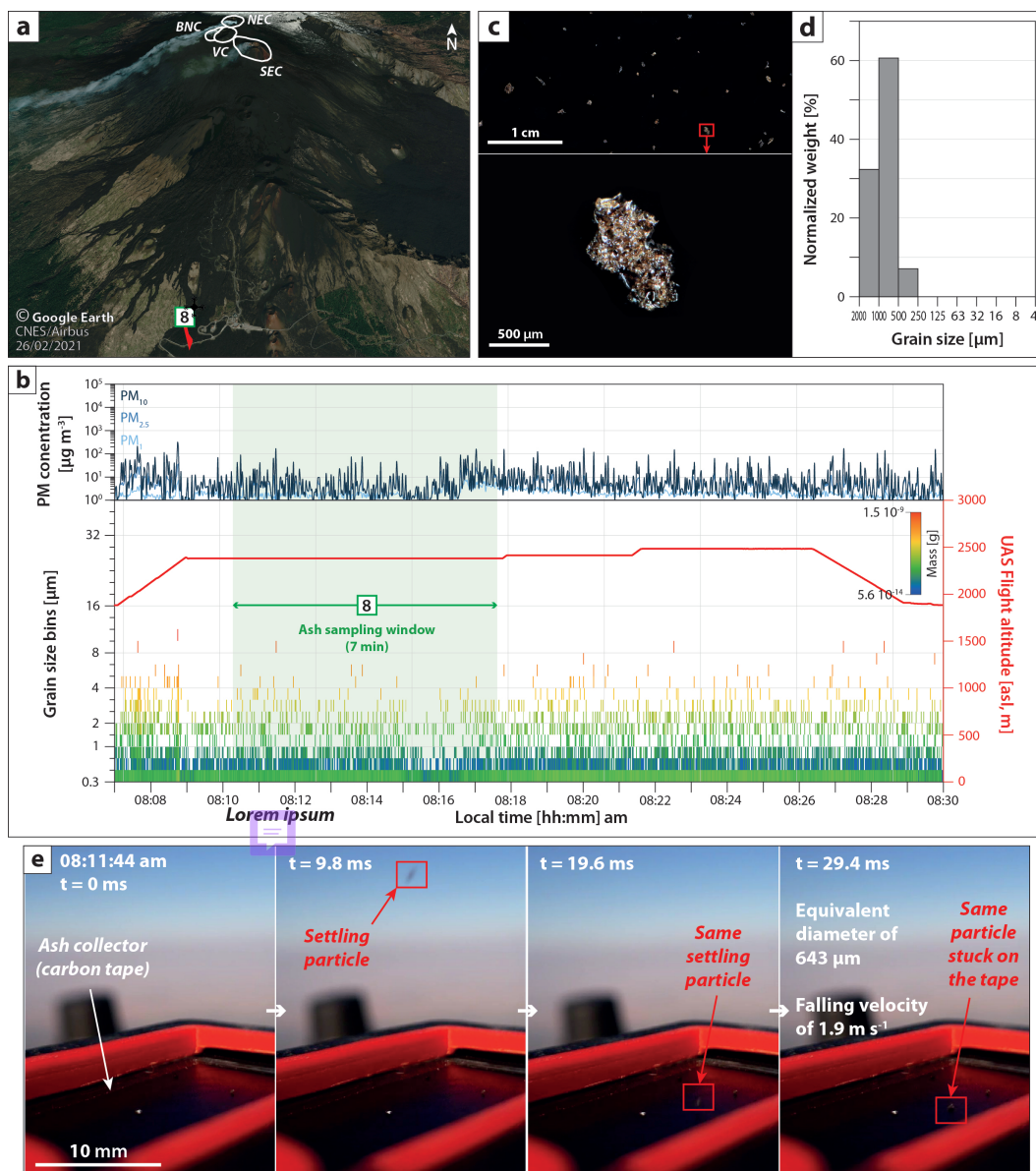
Figure 8. Results obtained by the A_2C_3 device for the 23th of July 2024 paroxysmal eruption at Etna. (a) UAV flight path (red line) during which the optical particle counter (OPC) analysis was performed. The green square labeled 8 corresponds to the site shown in Figures 4c and 5c, and represents the ash sampling location and duration (also shown in b). White lines delimit the summit craters shown in Figure 5b (BNC: Bocca Nuova crater; VC: Voragine crater; NEC: North-east crater; SEC: South-east crater). (b) Particulate matter (PM) concentrations and grain size spectrogram from the optical particle counter (OPC) data. (c) Optical microscopy images of the collected sample at different scales.(d) Grain Size Distribution (GDS) inferred from image analysis of the collected sample. (e) Sequence example of a single ash fallout particle imaged by the camera, with annotated equivalent diameter and settling velocity (the full video is available in the supplementary material). Note that the farthest corner of the samping area corresponds to the top right corner of the sample image shown in c. The particle framed in red corresponds to the particle shown in (c).

17

identified to directly fall and stick in the ash collector (cf. red square in Figure 8e, cf. also supplementary material, File S6, for

360 raw data). This particle has an estimated falling velocity of 1.9 m s^{-1} and an average diameter of 643 µm (in agreement with

the Figure 8c that shows the same particle in the ash collector).

3.4 Fourth case study: atmospheric analysis with the multigas detector inside the gas-rich cloud of the 19th of November 2023

The fourth ~~and last~~ case study is ~~described~~ based on a 15.6 min-long UAV flight, along the trajectory shown in Figure 9a (cf.

365 also supplementary material, File S2, for the UAV flight report). The multigas analysis has been cropped to the maximum flight

altitude of 589 m asl to show acquired data during a horizontal flight at a steady altitude, trying to cover the area of the base

of the gas-rich cloud. This represents a 9-min long and continuous atmospheric analysis (Figure 9b, cf. also supplementary

material, File S7, for raw data).
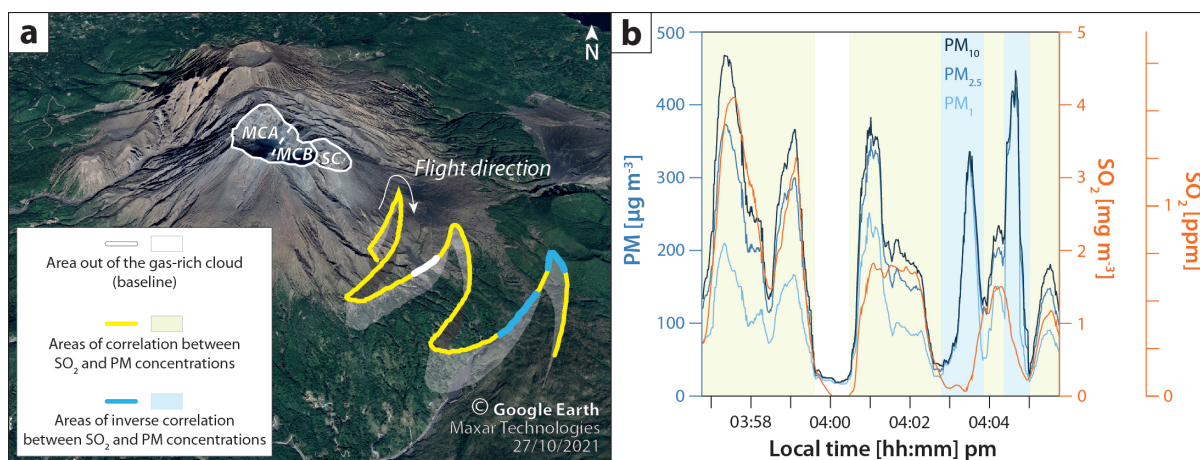
Figure 9. Results obtained by the multigas detector. White lines delimit the active craters shown in Figure 3b (MCA: Minamidake crater vent A; MCB: Minamidake crater vent B; SC: Showa crater). (a) UAV flight path during the multigas analysis for the 19th of November 2023 continuous degassing period (cf. Figures 3c and 5d). (b) Particulate matter (PM) and sulfur dioxide (SO$_2$) concentrations are a function of time. Note that time is directly correlated to the UAS location shown in a, as the UAV flew at the steadiest horizontal speed as possible (65 ±21 km h^{-1}).

CO$_2$ concentrations are steady during the entire multigas analysis (between 0.06 and 0.07 %), as well as T (between 4 and 6

370 °C) and RH (between 51 and 59 %). Nevertheless, high variations in SO$_2$ and PM concentrations are observed, and acquired

data can be classified into three different areas. (i) One small part of the multigas analysis was measuring atmospheric baseline

out of the gas-rich cloud (white line and area in Figure 9), as SO$_2$ concentrations are at 0 ppm and PM concentrations at

baseline levels (i.e., lower than 40 µg m^{-3} for PM$_1$, PM$_{2.5}$, and PM$_{10}$). (ii) The main part of the multigas analysis showed cloud

areas where SO$_2$ and PM concentrations are correlated (yellow lines and areas in Figure 9). SO$_2$ concentrations are measured

375 up to 1.4 ppm with PM$_1$, PM$_{2.5}$, and PM$_{10}$ concentrations up to 250, 380, and 470 µg m^{-3}, respectively. (iii) Most interestingly,

Atmospheric
Measurement
Techniques
Discussions

some of the parts of the multigas analysis scoped cloud areas where SO_2 and PM concentrations are inversely correlated (blue lines and areas in Figure 9). More specifically, these areas show a sudden increase of PM concentrations (up to ca. 450 µg m^{-3} for PM_1, $PM_{2.5}$, and PM_{10}) with relatively low level of SO_2 (down to 0.2 ppm).

4 Discussion

380 ### 4.1 Different OPC and sample signatures inside and below ash-loaded clouds as revealed by the A_2C_2 and A_2C_3 devices

OPC data acquired outside the volcanic cloud on the 10th of November 2023 (Figure 6b) is characterized by low PM concentrations (PM_{10} lower than 40 µg m^{-3}) in accordance with the ones generally measured in the ambient atmosphere (e.g., Dongarrà et al., 2010; Filonchyk et al., 2016; Morino et al., 2018). The fact that PM baseline values after the cloud interception are 385 slightly higher (PM_{10} up to 100 µg m^{-3}) than the beginning of the measurement, either suggests that the volcanic cloud left some slight traces of fine particles in the atmosphere on the UAS trip back to base, or that the OPC needs some time to balance and clean itself after passing through areas with high particle concentrations.

Nevertheless, these relatively low baseline concentrations contrast with the higher ones measured inside the ash-loaded cloud on the 10th of November 2023 (PM_{10} up to 80000 µg m^{-3}, cf. Figure 6b), which are significantly above the guidelines of 390 daily (250 µg m^{-3}) and annual (150 µg m^{-3}) maximum exposures to PM_{10} provided by the international volcanic health hazard network (IVHHN, https://www.ivhhn.org/index.php/). Even though more regular measurements are required in order to assess the real evolution of PM_{10} values during these durations, this is important to note as a downslope wind brought this cloud at low altitudes, which often occurs in the Sakurajima area (Poulidis et al., 2017), resulting in potential high PM concentration exposures at ground level. The lifetime of the high PM concentration anomaly (ca. 4 minutes and segmented into two parts 395 probably because the UAS was at the edge of the cloud) agrees with the fact that the OPC was intercepting the ash-loaded cloud (Figure 5a). We interpret the unlikely lack of PM_1 and $PM_{2.5}$ at the beginning and the end of the cloud interception (Figure 6b) as a hardware bias because previous laboratory tests showed that the OPC displays null or unusual small values when measuring extreme concentrations of small particles. Note that another OPC bias can also occur when the UAS moves due to the orientation of the OPC, which sucks air that is moving perpendicular to its inlet. In this setup, the particle sampling 400 bias worsens as the particle gets larger (i.e., non-isokinetic sampling). However, the recorded data suggest that this bias is not significant compared to the real variations observed in the atmosphere.

Another interesting pattern was identified when the UAS reached the ash fallout area below the volcanic cloud on the 11th of November 2023 (Figure 7b) at Sakurjima. Instead of a single and global increase of PM concentrations as observed when intercepting the ash-loaded cloud, zones below the cloud are characterized by spontaneous and brief increases of GSD modes 405 and PM concentrations (PM_{10} up to 3000 µg m^{-3}), not as high as in the cloud but still above the IVHHN guidelines, emphasizing that even low-intensity events represent potential health risk respiratory downwind the event source. We interpret the short-lived GSD mode and PM peaks as representative of ash fallout with a pulsatory behavior, either corresponding to the source (i.e., pulsatory nature of the explosive event, cf. Figure 5b) and/or to sedimentation processes, such as SDGIs generating discrete

ash fingers (e.g., Scollo et al., 2017; Freret-Lorgeril et al., 2020; Lemus et al., 2021; Fries et al., 2021). The homogeneous
410 particle distribution on the tape (Figure 7c) agrees that the collected particles were settling vertically without any significant turbulence, in accordance with an ash fallout laminar regime (Bonadonna et al., 2015). Interestingly, the OPC measurement in the fallout area of Etna shows only a baseline pattern, suggesting the absence of fine particles.

The combined results from the OPC measurements and the laboratory analysis of the collected samples enable more insights into the real GSD of the investigated areas. At Sakurajima, particle counts from the OPC show a systematic fine mode (between
415 4 and 16 μm), both inside the cloud and in the fallout area, while a coarser mode is systematically observed from the image analysis of the associated samples, between 63 and 125 μm excluding ash aggregates that can be coarser up to 500 μm (Figures 6 and 7). Note that Sakurajima and Etna fallout samples were collected 2 and 6 km away, respectively (Figures 3 and 4). Even though, the Etna fallout sample (Figure 8) is coarser (mode between 500 and 1000 μm) than the Sakurajima ones (coarse mode between 63 and 125 μm excluding aggregates), suggesting different eruptive parameters and transport mechanisms.

420 In addition, the significant occurrence of particle aggregates in the Sakurajima samples (absent for Etna sample), and more specifically in the fallout sample, confirms that aggregation is a common feature at Sakurajima (e.g., Gilbert et al., 1991; Bagheri et al., 2016; Diaz-Vecino et al., 2022). The observed aggregates are all PC types, in agreement with the absence of rain or significant amounts of condensed water in the atmosphere during the studied events (Figures 5a and b). Also, the fact that most of the sampled fallout particles are part of structured aggregates (Figure 7c) confirms that this UAS sampling is efficient
425 for the sampling of aggregated particles despite their fragile nature (i.e., no significant turbulence generated in the upper side of the UAS). The grain size mode of the Sakurajima fallout sample (between 250 and 500 μm) is mostly composed of aggregates. Therefore, a more detailed image analysis (i.e., manual separation of single particles inside aggregates) should be performed to better investigate ash aggregation and get a real GSD considering both single and aggregated particles. The use of ash collectors with resin is also shown to better preserve the aggregate structures compared to carbon tape (Bagheri et al., 2016; Diaz-Vecino
430 et al., 2022; Gabellini et al., 2024) and need to be tested in the future with the A_2C_3 device, which enables a visual monitoring of falling particles. Even though more data need to be acquired, falling velocity falls estimated at Etna falls in the expected range for the observed particle size and texture (Freret-Lorgeril et al., 2019, 2020). This suggests that drone turbulence is not affecting ash sedimentation.

4.2 The complexity of gas-rich clouds as revealed by the multigas detector

435 First, note that the different exposure times of the different multigas sensors is not critical for data interpretation as data shows on multiple occasions that SO_2 and PM concentrations are well correlated (Figure 9b). Interestingly, the UAV flight carrying multigas analysis in the gas-rich cloud on the 19th of November 2023 sometimes shows high PM concentrations, highlighting that continuous degassing clouds also involved fine ash particles that were probably emitted and remobilized at the source (i.e., ash venting). PM concentrations also strongly oscillated (sometimes PM and SO2 are anti-correlated) probably because
440 ash venting experienced variable efficiencies in the production of particles. The relatively low expected Stokes number of PM particles (significantly below 1) supports that PM particles are mostly tracers and behave like gases (drag-dominated regime), and most likely exclude a potential decoupling between SO_2 and PM particles during the volcanic cloud transport.

Even though more measurements and quantification of the relevant parameters (e.g., cloud velocity and turbulence, as well as particle sedimentation rate) are needed, we suggest that these areas of high particle concentrations could eventually lead PM_{10}

445 and coarser particles to aggregate and/or sediment by gravity, ultimately forming discrete areas of particle sedimentation when low levels of turbulence are reached.

It is also important to note that both SO_2 (up to 1.4 ppm) and PM (PM_{10} up to 470 µg m^{-3}) concentrations were most of the time above the hourly (1 ppm of SO_2), daily (0.153 ppm of SO_2), and annual (0.038 ppm of SO_2) maximum of exposure provided by the IVHHN guidelines, as the base of the cloud was sometimes, and in some areas, brought at ground levels by

450 downslope winds (Figure 5c). Similarly to PM_{10} concentrations, more continuous measurements are nonetheless necessary to evaluate the evolution of SO_2 concentrations and rigorously assess potential health threats induced by SO_2 at Sakurajima.

5   Conclusions and perspectives

Our study highlights that the developed and acquired technologies (Figures 1 and 2) can be used to study various types of volcanic phenomena (Figures 3 and 5). Depending on the site accessibility, UAV local flight regulations, and atmospheric con-

455 ditions, the approach shown here enables in-situ ash sampling, and the measurements of GSDs, as well as PM_1, $PM_{2.5}$, PM_{10}, SO_2, and CO_2 concentrations inside (Figures 6, 9, 10a and c) and below (Figures 7 and 10b) ash- and/or gas-rich volcanic clouds. Exploratory results acquired in November 2023 at Sakurajima volcano and in July 2024 at Etna evidence significant differences between baseline (low PM concentrations, e.g., below 30 µg m^{-3} for PM_{10}), inside- (high PM concentrations, e.g., up to 80000 µg m^{-3} for PM_{10}, limited particle aggregation) and below-cloud (intermediate PM concentration, e.g., up to 3000

460 µg m^{-3}, well-developed particle aggregation at Sakurajima, not observed at Etna) environments. Hence, a wide range of opportunities opens to study volcanic events, as acquired airborne samples and atmospheric data can be studied for various purposes, from understanding the origins and mechanisms of volcanic eruptions to deciphering their potential impacts. Hereafter, we provide some areas where the use and integration of UAS-related measurements could be implemented to support volcanic hazard forecasting and risk mitigation.

465 (i) UAV flights allow us to reach remote and/or hazardous areas (Figures 3c and 5). Hence, UAS-related results represent invaluable complementary data and sample acquisition to the information collected by classical field works at ground level, static monitoring stations, and monitoring networks, as well as various remote sensing methods and crowd-sourced studies implying local population observation and sampling (e.g., Bonadonna et al., 2012; Thivet et al., 2020b; Balangue-Tarriela et al., 2022).

470 (ii) The A_2C, the A_2C_2, and mostly the A_2C_3 devices represent an innovative instrumentation to collect and characterize particles directly in the atmosphere. These represent a new complementary technique to in-situ imaging (Lawson et al., 2006), especially for coarse particles larger than 40 µm. The unique combination of aerosol measurements (OPC), ash collection (sampler), and camera is a step forward to fill knowledge gaps concerning key eruptive parameters (i.e., GSDs, particle concentrations) and sedimentation processes (i.e., particle aggregation, SDGIs) during the transport and sedimentation of volcanic

475 ash (e.g., Rose and Durant, 2011; Brown et al., 2012; Rossi et al., 2021). For instance, more sampling (with associated image

Atmospheric
Measurement
Techniques
Open Access
EGU
Discussions
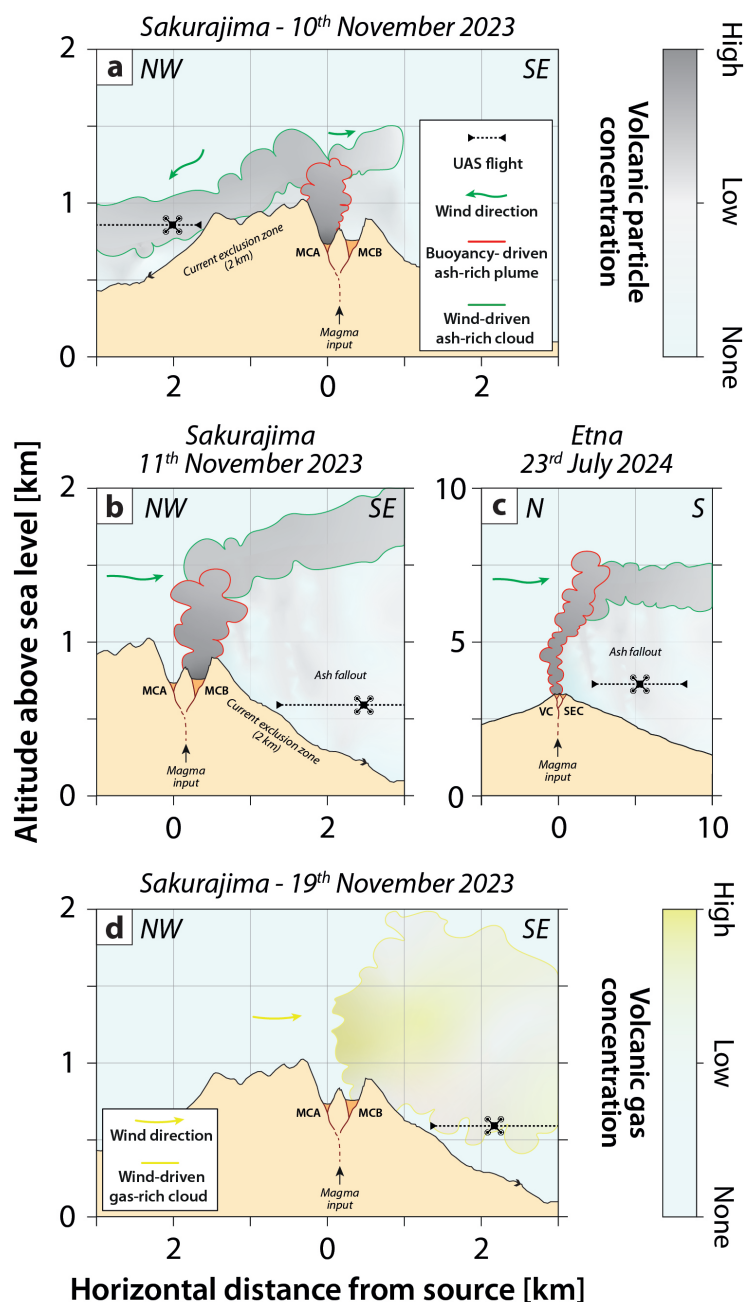
Figure 10. The different case studies and possible applications shown in this study. (a) In-situ analysis and sampling inside ash-loaded volcanic clouds: example of the 10th of November 2023 at Sakurajima. (b) In-situ analysis and sampling of ash fallout below volcanic clouds: example of the 11th of November 2023 at Sakurajima. (c) In-situ analysis and sampling of ash fallout below volcanic clouds: example of the 23th of July 2024 at Etna.(d) In-situ analysis of gas-rich volcanic clouds: example of the 19th of November 2023 at Sakurajima.

analysis of samples) and atmospheric analyses both in air and at ground level need to be performed to investigate the occurrence of particle aggregation during ash fallout (Figure 7c) and inside cloud samples (Figure 6c). Note that the instrumentation shown in this study can potentially be adapted for other UAV models and dedicated to monitoring at ground level. A$_2$C can be used to validate and test different sampling methods, as it displays two sampling slots (one can be used with an adhesive carbon

480   tape, another can be used with UV resin, cf. also Figure 2a and b). However, A$_2$C$_2$, and A$_2$C$_3$ are mostly used for research purposes (Figure 2e) as they can sample and measure GSDs and PM concentrations simultaneously, also with *in-situ* visual monitoring (Figure 2c, d, e, f).

(iii) Supplementary laboratory analysis can also be performed on the collected samples (e.g., GSD inside aggregates, particle componentry, morphology, texture, and composition, cf. Gurioli et al. 2022), to better understand processes involved before,

485   during, and after eruptions. More specifically, conducting a standardized post-eruption analysis can provide a comprehensive understanding of the processes responsible for generating volcanic particles, and ultimately compare acquired datasets for different case studies (Ross et al., 2022).

(iv) The intricate interactions between ash particles and gases within volcanic clouds need to be further investigated, as they can result in unexpected and impactful processes, including the chemical reactions on ash surfaces, changes in particle aggre-

490   gation efficiencies, and the modification of gas compositions (e.g., Delmelle et al., 2007, 2018; Colombier et al., 2019). UAS devices represent an innovative and efficient approach to decipher these mechanisms, as sampling and analysis are accurately performed *in-situ*, inside or below volcanic clouds.

(v) Gas monitoring (more specifically for SO$_2$ and CO$_2$) is also important for eruption forecasting (e.g., Sparks, 2003; Aiuppa et al., 2007; Poland et al., 2020) and the characterisation of eruptive style transition (e.g., Shinohara et al., 2020; Thivet

495   et al., 2020a, 2021). Thus, UAS-based volcanic gas measurements and sampling can be useful to regularly monitor *in-situ* gas parameters in active volcanic sites as a complement to ground-based stations, especially above volcanic vents where permanent monitoring systems cannot be installed (e.g., Liu et al., 2019, 2020; Pering et al., 2020).

(vi) The A$_2$C$_3$ and multigas devices can be also useful to monitor air quality in various environments and conditions. They can be used to study, monitor, and warn about volcanic ash health impacts, as this hazard is well-known to cause consequences

500   on respiratory health (e.g., Horwell and Baxter, 2006; Hillman et al., 2012; Andronico and Del Carlo, 2016). The multigas device can be also used to scope emissions of volcanic gases, especially SO$_2$, as this gas is well-known for causing various health issues (e.g., Shinkura et al., 1999; Hansell and Oppenheimer, 2004; Schmidt et al., 2015) that can bring volcanic aerosols and gases at ground levels.

Data availability. All data used in this study is available in the supplementary material of this paper

505   *Sample availability.* All samples collected and used in this study are stored at the Department of Earth Sciences of the University of Geneva, Switzerland

Video supplement. One video is available in the supplementary material of this paper

Author contributions. S. Thivet prepared and piloted the UAV during the field campaigns, analyzed the data collected by the UAS, and wrote the first draft of the paper. C. Bonadonna, G. Bagheri, J. Lemus, A. Fries, and E. Rossi initiated and designed the initial project of the UAS

510 application for in-situ volcanic cloud exploration. P. M. Kornatowski advised the choice of the UAV and of the multigas detection hardware and designed the A_2C and A_2C_2 instruments. A. Fries, S. Thivet and R. Simionato developed the UAS-embedded A_2C_3 instrument. S. Scollo, R. Simionato and C. Díaz-Vecino collected and analyzed the videos of the volcanic events during the field campaign. T. Yamada assisted us at Sakurajima. S. Scollo assisted us at Etna. All authors contributed to the finalization of the paper.

Competing interests. The authors declare no competing interests.

References

Aiuppa, A., Moretti, R., Federico, C., Giudice, G., Gurrieri, S., Liuzzo, M., Papale, P., Shinohara, H., and Valenza, M.: Forecasting Etna eruptions by real-time observation of volcanic gas composition, Geology, 35, 1115–1118, https://doi.org/10.1130/G24149A.1, 2007.

520 Allison, R. S., Johnston, J. M., Craig, G., and Jennings, S.: Airborne Optical and Thermal Remote Sensing for Wildfire Detection and Monitoring, Sensors, 16, 1310, https://doi.org/10.3390/s16081310, 2016.

Andronico, D. and Del Carlo, P.: PM_{10} measurements in urban settlements after lava fountain episodes at Mt. Etna, Italy: pilot test to assess volcanic ash hazard to human health, Natural Hazards and Earth System Sciences, 16, 29–40, https://doi.org/10.5194/nhess-16-29-2016, 2016.

525 Andò, B., Baglio, S., Castorina, S., Graziani, S., Claudio, L., Marletta, V., and Trigona, C.: An Embedded Vision Tool for Volcanic Ash Analysis, in: 2021 IEEE Sensors Applications Symposium (SAS), pp. 1–5, https://doi.org/10.1109/SAS51076.2021.9530027, 2021.

Antoine, R., Lopez, T., Tanguy, M., Lissak, C., Gailler, L., Labazuy, P., and Fauchard, C.: Geoscientists in the Sky: Unmanned Aerial Vehicles Responding to Geohazards, Surveys in Geophysics, 41, 1285–1321, https://doi.org/10.1007/s10712-020-09611-7, 2020.

Bagheri, G., Rossi, E., Biass, S., and Bonadonna, C.: Timing and nature of volcanic particle clusters based on field and numerical investiga-
530 tions, Journal of Volcanology and Geothermal Research, 327, 520–530, https://doi.org/10.1016/j.jvolgeores.2016.09.009, 2016.

Balangue-Tarriela, M. I. R., Lagmay, A. M. F., Sarmiento, D. M., Vasquez, J., Baldago, M. C., Ybañez, R., Ybañez, A. A., Trinidad, J. R., Thivet, S., Gurioli, L., De Vries, B. V. W., Aurelio, M., Rafael, D. J., Bermas, A., and Escudero, J. A.: Analysis of the 2020 Taal Volcano tephra fall deposits from crowdsourced information and field data, Bulletin of Volcanology, 84, 35, https://doi.org/10.1007/s00445-022-01534-y, 2022.

535 Bellingham, J. G. and Rajan, K.: Robotics in Remote and Hostile Environments, Science, 318, 1098–1102, https://doi.org/10.1126/science.1146230, 2007.

Boccardo, P., Chiabrando, F., Dutto, F., Tonolo, F. G., and Lingua, A.: UAV Deployment Exercise for Mapping Purposes: Evaluation of Emergency Response Applications, Sensors, 15, 15 717–15 737, https://doi.org/10.3390/s150715717, 2015.

Bonadonna, C., Genco, R., Gouhier, M., Pistolesi, M., Cioni, R., Alfano, F., Hoskuldsson, A., and Ripepe, M.: Tephra sedimentation during
540 the 2010 Eyjafjallajökull eruption (Iceland) from deposit, radar, and satellite observations, Journal of Geophysical Research: Solid Earth, 116, https://doi.org/10.1029/2011JB008462, 2011.

Bonadonna, C., Folch, A., Loughlin, S., and Puempel, H.: Future developments in modelling and monitoring of volcanic ash clouds: outcomes from the first IAVCEI-WMO workshop on Ash Dispersal Forecast and Civil Aviation, Bulletin of Volcanology, 74, 1–10, https://doi.org/10.1007/s00445-011-0508-6, 2012.

545 Bonadonna, C., Costa, A., Folch, A., and Koyaguchi, T.: Chapter 33 - Tephra Dispersal and Sedimentation, in: The Encyclopedia of Volcanoes (Second Edition), edited by Sigurdsson, H., pp. 587–597, Academic Press, Amsterdam, ISBN 978-0-12-385938-9, https://www.sciencedirect.com/science/article/pii/B978012385938900033X, 2015.

Bonadonna, C., Biass, S., Menoni, S., and Gregg, C. E.: Chapter 8 - Assessment of risk associated with tephra-related hazards, in: Forecasting and Planning for Volcanic Hazards, Risks, and Disasters, edited by Papale, P., vol. 2 of *Hazards and Disasters Series*, pp. 329–378,
550 Elsevier, ISBN 978-0-12-818082-2, https://www.sciencedirect.com/science/article/pii/B9780128180822000081, 2021.

Brosch, E.: Volcanic Ash and Small Uncrewed Aerial Vehicle (sUAV) Interaction: In-situ Observations and Laboratory Experiments on Aircraft Failure, Frontiers in Earth Science, 10, 810 962, https://doi.org/10.3389/feart.2022.810962, 2022.

Brown, R. J., Bonadonna, C., and Durant, A. J.: A review of volcanic ash aggregation, Physics and Chemistry of the Earth, Parts A/B/C, 45-46, 65–78, https://doi.org/10.1016/j.pce.2011.11.001, 2012.

555 Calvari, S., Cannavò, F., Bonaccorso, A., Spampinato, L., and Pellegrino, A. G.: Paroxysmal Explosions, Lava Fountains and Ash Plumes at Etna Volcano: Eruptive Processes and Hazard Implications, Frontiers in Earth Science, 6, https://doi.org/10.3389/feart.2018.00107, 2018.

Carreño Ruiz, M., Bloise, N., Guglieri, G., and D'Ambrosio, D.: Numerical Analysis and Wind Tunnel Validation of Droplet Distribution in the Wake of an Unmanned Aerial Spraying System in Forward Flight, Drones, 6, 329, https://doi.org/10.3390/drones6110329, 2022.

Civico, R., Ricci, T., Scarlato, P., Andronico, D., Cantarero, M., Carr, B. B., De Beni, E., Del Bello, E., Johnson, J. B., Kueppers, U.,
560 Pizzimenti, L., Schmid, M., Strehlow, K., and Taddeucci, J.: Unoccupied Aircraft Systems (UASs) Reveal the Morphological Changes at Stromboli Volcano (Italy) before, between, and after the 3 July and 28 August 2019 Paroxysmal Eruptions, Remote Sensing, 13, 2870, https://doi.org/10.3390/rs13152870, 2021.

Colombier, M., Mueller, S. B., Kueppers, U., Scheu, B., Delmelle, P., Cimarelli, C., Cronin, S. J., Brown, R. J., Tost, M., and Dingwell, D. B.: Diversity of soluble salt concentrations on volcanic ash aggregates from a variety of eruption types and deposits, Bulletin of Volcanology,
565 81, 39, https://doi.org/10.1007/s00445-019-1302-0, 2019.

Costa, D., Burlando, P., and Priadi, C.: The importance of integrated solutions to flooding and water quality problems in the tropical megacity of Jakarta, Sustainable Cities and Society, 20, 199–209, https://doi.org/10.1016/j.scs.2015.09.009, 2016.

Del Rosso, M. P., Sebastianelli, A., Spiller, D., Mathieu, P. P., and Ullo, S. L.: On-Board Volcanic Eruption Detection through CNNs and Satellite Multispectral Imagery, Remote Sensing, 13, 3479, https://doi.org/10.3390/rs13173479, 2021.

570 Delmelle, P.: Environmental impacts of tropospheric volcanic gas plumes, in: Volcanic Degassing, edited by Oppenheimer, C., Pyle, D. M., and Barclay, J., vol. 213, p. 0, Geological Society of London, ISBN 978-1-86239-136-9, https://doi.org/10.1144/GSL.SP.2003.213.01.23, 2003.

Delmelle, P., Lambert, M., Dufrêne, Y., Gerin, P., and Óskarsson, N.: Gas/aerosol–ash interaction in volcanic plumes: New insights from surface analyses of fine ash particles, Earth and Planetary Science Letters, 259, 159–170, https://doi.org/10.1016/j.epsl.2007.04.052, 2007.

575 Delmelle, P., Wadsworth, F. B., Maters, E. C., and Ayris, P. M.: High Temperature Reactions Between Gases and Ash Particles in Volcanic Eruption Plumes, Reviews in Mineralogy and Geochemistry, 84, 285–308, https://doi.org/10.2138/rmg.2018.84.8, 2018.

Diaz-Vecino, C., Rossi, E., Freret-Lorgeril, V., Fries, A., Gabellini, P., Lemus, J., Pollastri, S., Poulidis, A. P., Iguchi, M., and Bonadonna, C.: Aerodynamic characteristics and genesis of aggregates at Sakurajima Volcano, Japan, Scientific Reports, 12, 2044, https://doi.org/10.1038/s41598-022-05854-z, 2022.

580 Diaz-Vecino, C., Rossi, E., Pollastri, S., Fries, A., Lemus, J., and Bonadonna, C.: Insights into the sticking probability of volcanic ash particles from laboratory experiments, Scientific Reports, 13, 21 188, https://doi.org/10.1038/s41598-023-47712-6, 2023.

Dongarrà, G., Manno, E., Varrica, D., Lombardo, M., and Vultaggio, M.: Study on ambient concentrations of PM10, PM10–2.5, PM2.5 and gaseous pollutants. Trace elements and chemical speciation of atmospheric particulates, Atmospheric Environment, 44, 5244–5257, https://doi.org/10.1016/j.atmosenv.2010.08.041, 2010.

585 Eliasson, J., Watson, I. M., and Weber, K.: Chapter 5 - In Situ Observations of Airborne Ash From Manned Aircraft, in: Volcanic Ash, edited by Mackie, S., Cashman, K., Ricketts, H., Rust, A., and Watson, M., pp. 89–98, Elsevier, ISBN 978-0-08-100405-0, https://www.sciencedirect.com/science/article/pii/B9780081004050000094, 2016.

Ferlito, C., Bruno, V., Salerno, G., Caltabiano, T., Scandura, D., Mattia, M., and Coltorti, M.: Dome-like behaviour at Mt. Etna: The case of the 28 December 2014 South East Crater paroxysm, Scientific Reports, 7, 5361, https://doi.org/10.1038/s41598-017-05318-9, 2017.

590   Fernandez Galarreta, J., Kerle, N., and Gerke, M.: UAV-based urban structural damage assessment using object-based image analysis and semantic reasoning, Natural Hazards and Earth System Sciences, 15, 1087–1101, https://doi.org/10.5194/nhess-15-1087-2015, 2015.

Filonchyk, M., Yan, H., Yang, S., and Hurynovich, V.: A study of PM2.5 and PM10 concentrations in the atmosphere of large cities in Gansu Province, China, in summer period, Journal of Earth System Science, 125, 1175–1187, https://doi.org/10.1007/s12040-016-0722-x, 2016.

Flagan, R. C. and Seinfeld, J. H.: Fundamentals of air pollution engineering, Courier Corporation, https://books.google.com/
595   books?hl=fr&lr=&id=-YZHbjUo9lAC&oi=fnd&pg=PP1&dq=Fundamentals+of+air+pollution+engineering&ots=zg8YiNNaQq&
sig=7LIMkaIjc-jbI7sZ3awn_yKU6yU, 2012.

Folch, A.: A review of tephra transport and dispersal models: Evolution, current status, and future perspectives, Journal of Volcanology and Geothermal Research, 235-236, 96–115, https://doi.org/10.1016/j.jvolgeores.2012.05.020, 2012.

Freret-Lorgeril, V., Donnadieu, F., Eychenne, J., Soriaux, C., and Latchimy, T.: In situ terminal settling velocity measurements at
600   Stromboli volcano: Input from physical characterization of ash, Journal of Volcanology and Geothermal Research, 374, 62–79, https://doi.org/10.1016/j.jvolgeores.2019.02.005, 2019.

Freret-Lorgeril, V., Gilchrist, J., Donnadieu, F., Jellinek, A., Delanoë, J., Latchimy, T., Vinson, J., Caudoux, C., Peyrin, F., Hervier, C., and Valade, S.: Ash sedimentation by fingering and sediment thermals from wind-affected volcanic plumes, Earth and Planetary Science Letters, 534, 116 072, https://doi.org/10.1016/j.epsl.2020.116072, 2020.

605   Freret-Lorgeril, V., Bonadonna, C., Rossi, E., Poulidis, A. P., and Iguchi, M.: New insights into real-time detection of tephra grainsize, settling velocity and sedimentation rate, Scientific Reports, 12, 4650, https://doi.org/10.1038/s41598-022-08711-1, 2022.

Fries, A., Lemus, J., Jarvis, P. A., Clarke, A. B., Phillips, J. C., Manzella, I., and Bonadonna, C.: The Influence of Particle Concentration on the Formation of Settling-Driven Gravitational Instabilities at the Base of Volcanic Clouds, Frontiers in Earth Science, 9, 640 090, https://doi.org/10.3389/feart.2021.640090, 2021.

610   Fries, A., Dominguez, L., Jarvis, P. A., Pistolesi, M., Manrique, N., Aguilar, R., Valdivia, D., Rossi, E., Pollastri, S., Horwell, C. J., and Bonadonna, C.: The post-2016 long-lasting Vulcanian activity of Sabancaya volcano (Peru) and associated aeolian remobilisation of volcanic ash, Journal of Volcanology and Geothermal Research, 441, 107 876, https://doi.org/10.1016/j.jvolgeores.2023.107876, 2023.

Funaki, M., Higashino, S.-I., Sakanaka, S., Iwata, N., Nakamura, N., Hirasawa, N., Obara, N., and Kuwabara, M.: Small unmanned aerial vehicles for aeromagnetic surveys and their flights in the South Shetland Islands, Antarctica, Polar Science, 8, 342–356,
615   https://doi.org/10.1016/j.polar.2014.07.001, 2014.

Gabellini, P., Cioni, R., Geshi, N., Pistolesi, M., Miwa, T., Lacanna, G., and Ripepe, M.: Eruptive dynamics and fragmentation mechanisms during cyclic Vulcanian activity at Sakurajima volcano (Japan): Insights from ash texture analysis, Journal of Volcanology and Geothermal Research, 428, 107 582, https://doi.org/10.1016/j.jvolgeores.2022.107582, 2022.

Gabellini, P., Rossi, E., Cioni, R., Pistolesi, M., Baumgartner, L., and Bonadonna, C.: The Hidden Structure of Volcanic Ash Aggregates as
620   Unveiled by X-ray Micro-tomography, 2024.

Gailler, L., Labazuy, P., Régis, E., Bontemps, M., Souriot, T., Bacques, G., and Carton, B.: Validation of a New UAV Magnetic Prospecting Tool for Volcano Monitoring and Geohazard Assessment, Remote Sensing, 13, 894, https://doi.org/10.3390/rs13050894, 2021.

Gailler, L., Labazuy, P., Régis, E., Peltier, A., and Ferrazzini, V.: Active structures and thermal state of the Piton de la Fournaise summit revealed by combined UAV magnetic and thermal infrared measurements, Volcanica, 5, 61–74, https://doi.org/10.30909/vol.05.01.6174,
625   2022.

Gao, M., Hugenholtz, C. H., Fox, T. A., Kucharczyk, M., Barchyn, T. E., and Nesbit, P. R.: Weather constraints on global drone flyability, Scientific Reports, 11, 12 092, https://doi.org/10.1038/s41598-021-91325-w, 2021.

Gilbert, J. S., Lane, S. J., Sparks, R. S. J., and Koyaguchi, T.: Charge measurements on particle fallout from a volcanic plume, Nature, 349, 598–600, https://doi.org/10.1038/349598a0, 1991.

630 Giordan, D., Manconi, A., Facello, A., Baldo, M., dell'Anese, F., Allasia, P., and Dutto, F.: Brief Communication: The use of an unmanned aerial vehicle in a rockfall emergency scenario, Natural Hazards and Earth System Sciences, 15, 163–169, https://doi.org/10.5194/nhess-15-163-2015, 2015.

Giordan, D., Hayakawa, Y., Nex, F., Remondino, F., and Tarolli, P.: Review article: the use of remotely piloted aircraft systems (RPASs) for natural hazards monitoring and management, Natural Hazards and Earth System Sciences, 18, 1079–1096, https://doi.org/10.5194/nhess-635 18-1079-2018, 2018.

Godfrey, I., Brenes, J. P. S., Cruz, M. M., Avard, G., and Meghraoui, K.: Launching the SnifferV and Sniffer4D multigas detectors into the active crater of the Poás Volcano in Costa Rica using unmanned aerial systems, Advanced UAV, 3, 153–176, https://publish.mersin.edu.tr/index.php/uav/article/view/1210, 2023.

Gurioli, L., Tadini, A., Thivet, S., Médard, E., Berthod, C., and Vlastélic, I.: Monitoring of Eruptive Products: Deposits Associated with 640 Pyroclastic Fallout, pp. 45–166, ISBN 978-1-78945-046-0, 2022.

Guéhenneux, Y. and Gouhier, M.: HOTVOLC: the official French satellite-based service for operational monitoring and early warning of volcanic ash plumes, Bulletin of Volcanology, 86, 29, https://doi.org/10.1007/s00445-024-01716-w, 2024.

Hansell, A. and Oppenheimer, C.: Health Hazards from Volcanic Gases: A Systematic Literature Review, Archives of Environmental Health: An International Journal, 59, 628–639, https://doi.org/10.1080/00039890409602947, 2004.

645 Hersbach, H., Bell, B., Berrisford, P., Biavati, G., Horányi, A., Muñoz Sabater, J., Nicolas, J., Peubey, C., Radu, R., and Rozum, I.: ERA5 hourly data on pressure levels from 1979 to present, Copernicus climate change service (c3s) climate data store (cds), 10, https://doi.org/10.24381/cds.bd0915c6, 2023.

Hillman, S. E., Horwell, C. J., Densmore, A. L., Damby, D. E., Fubini, B., Ishimine, Y., and Tomatis, M.: Sakurajima volcano: a physico-chemical study of the health consequences of long-term exposure to volcanic ash, Bulletin of Volcanology, 74, 913–930, 650 https://doi.org/10.1007/s00445-012-0575-3, 2012.

Hirose, M., Xiao, Y., Zuo, Z., Kamat, V. R., Zekkos, D., and Lynch, J.: Implementation of UAV localization methods for a mobile post-earthquake monitoring system, in: 2015 IEEE Workshop on Environmental, Energy, and Structural Monitoring Systems (EESMS) Proceedings, pp. 66–71, https://doi.org/10.1109/EESMS.2015.7175854, 2015.

Horwell, C. J. and Baxter, P. J.: The respiratory health hazards of volcanic ash: a review for volcanic risk mitigation, Bulletin of Volcanology, 655 69, 1–24, https://doi.org/10.1007/s00445-006-0052-y, 2006.

Hwang, J. Y., Jung, M. K., and Kwon, O. J.: Numerical Study of Aerodynamic Performance of a Multirotor Unmanned-Aerial-Vehicle Configuration, Journal of Aircraft, 52, 839–846, https://doi.org/10.2514/1.C032828, 2015.

Iguchi, M., Yamada, T., and Tameguri, T.: Sequence of Volcanic Activity of Sakurajima Volcano, Japan, as Revealed by Non-Eruptive Deflation, Frontiers in Earth Science, 10, https://doi.org/10.3389/feart.2022.727909, 2022.

660 Izumida, A., Uchiyama, S., and Sugai, T.: Application of UAV-SfM photogrammetry and aerial lidar to a disastrous flood: repeated topographic measurement of a newly formed crevasse splay of the Kinu River, central Japan, Natural Hazards and Earth System Sciences, 17, 1505–1519, https://doi.org/10.5194/nhess-17-1505-2017, 2017.

James, M. R., Carr, B., D'Arcy, F., Diefenbach, A., Dietterich, H., Fornaciai, A., Lev, E., Liu, E., Pieri, D., Rodgers, M., Smets, B., Terada, A., Von Aulock, F., Walter, T., Wood, K., and Zorn, E.: Volcanological applications of unoccupied aircraft systems (UAS): Developments, 665 strategies, and future challenges, Volcanica, 3, 67–114, https://doi.org/10.30909/vol.03.01.67114, 2020.

Jenkins, S. F., Wilson, T. M., Magill, C., Miller, V., Stewart, C., Blong, R., Marzocchi, W., Boulton, M., Bonadonna, C., and Costa, A.: Volcanic ash fall hazard and risk, Global volcanic hazards and risk, pp. 173–222, https://books.google.com/books?hl=fr&lr=&id=8loZCgAAQBAJ&oi=fnd&pg=PA173&dq=Jenkins+2015+Volcanic+ash+fall+hazard+and+risk,+Global+Volcanic+Hazard+and+Risk&ots=eOo64NrPve&sig=dE1aLhV1pHxu_xF3tgdTLuID8wA, 2015.

670 Jordan, B. R.: Collecting field data in volcanic landscapes using small UAS (sUAS)/drones, Journal of Volcanology and Geothermal Research, 385, 231–241, https://doi.org/10.1016/j.jvolgeores.2019.07.006, 2019.

Koyama, T., Kanda, W., Utsugi, M., Kaneko, T., Ohminato, T., Watanabe, A., Tsuji, H., Nishimoto, T., Kuvshinov, A., and Honda, Y.: Aeromagnetic survey in Kusatsu-Shirane volcano, central Japan, by using an unmanned helicopter, Earth, Planets and Space, 73, 139, https://doi.org/10.1186/s40623-021-01466-5, 2021.

675 Lawson, R. P., O'Connor, D., Zmarzly, P., Weaver, K., Baker, B., Mo, Q., and Jonsson, H.: The 2D-S (Stereo) Probe: Design and Preliminary Tests of a New Airborne, High-Speed, High-Resolution Particle Imaging Probe, https://doi.org/10.1175/JTECH1927.1, 2006.

Le Coz, J., Patalano, A., Collins, D., Guillén, N. F., García, C. M., Smart, G. M., Bind, J., Chiaverini, A., Le Boursicaud, R., Dramais, G., and Braud, I.: Crowdsourced data for flood hydrology: Feedback from recent citizen science projects in Argentina, France and New Zealand, Journal of Hydrology, 541, 766–777, https://doi.org/10.1016/j.jhydrol.2016.07.036, 2016.

680 Lemus, J., Fries, A., Jarvis, P. A., Bonadonna, C., Chopard, B., and Lätt, J.: Modelling Settling-Driven Gravitational Instabilities at the Base of Volcanic Clouds Using the Lattice Boltzmann Method, Frontiers in Earth Science, 9, 713 175, https://doi.org/10.3389/feart.2021.713175, 2021.

Lenton, T.: Earth System Science: A Very Short Introduction, Oxford University Press, ISBN 978-0-19-178833-8, https://academic.oup.com/book/558, 2016.

685 Lindner, G., Schraml, K., Mansberger, R., and Hübl, J.: UAV monitoring and documentation of a large landslide, Applied Geomatics, 8, 1–11, https://doi.org/10.1007/s12518-015-0165-0, 2016.

Liu, C.-C., Chen, P.-L., Matsuo, T., and Chen, C.-Y.: Rapidly responding to landslides and debris flow events using a low-cost unmanned aerial vehicle, Journal of Applied Remote Sensing, 9, 096 016, https://doi.org/10.1117/1.JRS.9.096016, 2015.

Liu, E. J., Wood, K., Mason, E., Edmonds, M., Aiuppa, A., Giudice, G., Bitetto, M., Francofonte, V., Burrow, S., Richardson, T., Watson, M., Pering, T. D., Wilkes, T. C., McGonigle, A. J. S., Velasquez, G., Melgarejo, C., and Bucarey, C.: Dynamics of Outgassing and Plume Transport Revealed by Proximal Unmanned Aerial System (UAS) Measurements at Volcán Villarrica, Chile, Geochemistry, Geophysics, Geosystems, 20, 730–750, https://doi.org/10.1029/2018GC007692, 2019.

Liu, E. J., Aiuppa, A., Alan, A., Arellano, S., Bitetto, M., Bobrowski, N., Carn, S., Clarke, R., Corrales, E., de Moor, J. M., Diaz, J. A., Edmonds, M., Fischer, T. P., Freer, J., Fricke, G. M., Galle, B., Gerdes, G., Giudice, G., Gutmann, A., Hayer, C., Itikarai, I., Jones, J.,

695 Mason, E., McCormick Kilbride, B. T., Mulina, K., Nowicki, S., Rahilly, K., Richardson, T., Rüdiger, J., Schipper, C. I., Watson, I. M., and Wood, K.: Aerial strategies advance volcanic gas measurements at inaccessible, strongly degassing volcanoes, Science Advances, 6, eabb9103, https://doi.org/10.1126/sciadv.abb9103, 2020.

Marchetti, E., Poggi, P., Donne, D. D., Pistolesi, M., Bonadonna, C., Bagheri, G., Pollastri, S., Thivet, S., Gheri, D., Gurioli, L., Harris, A., Hoskuldsoon, A., and Ripepe, M.: Real-time tephra-fallout accumulation rates and grain-size distributions using ASHER (ASH collector and sizER) disdrometers, Journal of Volcanology and Geothermal Research, 429, 107 611, https://doi.org/10.1016/j.jvolgeores.2022.107611, 2022.

Martínez-de Dios, J. R., Merino, L., Caballero, F., and Ollero, A.: Automatic Forest-Fire Measuring Using Ground Stations and Unmanned Aerial Systems, Sensors, 11, 6328–6353, https://doi.org/10.3390/s110606328, 2011.

29

Marzano, F. S., Picciotti, E., Montopoli, M., and Vulpiani, G.: Inside Volcanic Clouds: Remote Sensing of Ash Plumes Using Microwave
705   Weather Radars, https://doi.org/10.1175/BAMS-D-11-00160.1, 2013.

Mori, T., Hashimoto, T., Terada, A., Yoshimoto, M., Kazahaya, R., Shinohara, H., and Tanaka, R.: Volcanic plume measurements using a
UAV for the 2014 Mt. Ontake eruption, Earth, Planets and Space, 68, 49, https://doi.org/10.1186/s40623-016-0418-0, 2016.

Morino, Y., Chatani, S., Tanabe, K., Fujitani, Y., Morikawa, T., Takahashi, K., Sato, K., and Sugata, S.: Contributions of Con-
densable Particulate Matter to Atmospheric Organic Aerosol over Japan, Environmental Science & Technology, 52, 8456–8466,
710   https://doi.org/10.1021/acs.est.8b01285, 2018.

Neal, C. A., Brantley, S. R., Antolik, L., Babb, J. L., Burgess, M., Calles, K., Cappos, M., Chang, J. C., Conway, S., Desmither, L., Dotray,
P., Elias, T., Fukunaga, P., Fuke, S., Johanson, I. A., Kamibayashi, K., Kauahikaua, J., Lee, R. L., Pekalib, S., Miklius, A., Million, W.,
Moniz, C. J., Nadeau, P. A., Okubo, P., Parcheta, C., Patrick, M. R., Shiro, B., Swanson, D. A., Tollett, W., Trusdell, F., Younger, E. F.,
Zoeller, M. H., Montgomery-Brown, E. K., Anderson, K. R., Poland, M. P., Ball, J. L., Bard, J., Coombs, M., Dietterich, H. R., Kern, C.,
715   Thelen, W. A., Cervelli, P. F., Orr, T., Houghton, B. F., Gansecki, C., Hazlett, R., Lundgren, P., Diefenbach, A. K., Lerner, A. H., Waite, G.,
Kelly, P., Clor, L., Werner, C., Mulliken, K., Fisher, G., and Damby, D.: The 2018 rift eruption and summit collapse of Kīlauea Volcano,
Science, 363, 367–374, https://doi.org/10.1126/science.aav7046, 2019.

Paredes-Mariño, J., Forte, P., Alois, S., Chan, K. L., Cigala, V., Mueller, S. B., Poret, M., Spanu, A., Tomašek, I., Tournigand, P.-Y.,
Perugini, D., and Kueppers, U.: The lifecycle of volcanic ash: advances and ongoing challenges, Bulletin of Volcanology, 84, 51,
720   https://doi.org/10.1007/s00445-022-01557-5, 2022.

Pering, T. D., Liu, E. J., Wood, K., Wilkes, T. C., Aiuppa, A., Tamburello, G., Bitetto, M., Richardson, T., and McGonigle, A. J. S.: Com-
bined ground and aerial measurements resolve vent-specific gas fluxes from a multi-vent volcano, Nature Communications, 11, 3039,
https://doi.org/10.1038/s41467-020-16862-w, 2020.

Pering, T. D., Wilkes, T. C., Layana, S., Aguilera, F., and Aguilera, M.: The PiGas: A low-cost approach to volcanic gas sampling, Journal
725   of Volcanology and Geothermal Research, p. 108063, https://doi.org/10.1016/j.jvolgeores.2024.108063, 2024.

Poland, M. P., Lopez, T., Wright, R., and Pavolonis, M. J.: Forecasting, Detecting, and Tracking Volcanic Eruptions from Space, Remote
Sensing in Earth Systems Sciences, 3, 55–94, https://doi.org/10.1007/s41976-020-00034-x, 2020.

Poulidis, A. P., Takemi, T., Iguchi, M., and Renfrew, I. A.: Orographic effects on the transport and deposition of volcanic ash: A case study
of Mount Sakurajima, Japan, Journal of Geophysical Research: Atmospheres, 122, 9332–9350, https://doi.org/10.1002/2017JD026595,
730   2017.

Poulidis, A. P., Takemi, T., Shimizu, A., Iguchi, M., and Jenkins, S. F.: Statistical analysis of dispersal and deposition patterns of volcanic
emissions from Mt. Sakurajima, Japan, Atmospheric Environment, 179, 305–320, https://doi.org/10.1016/j.atmosenv.2018.02.021, 2018.

Román, A., Tovar-Sánchez, A., Roque-Atienza, D., Huertas, I. E., Caballero, I., Fraile-Nuez, E., and Navarro, G.: Unmanned aerial vehicles
(UAVs) as a tool for hazard assessment: The 2021 eruption of Cumbre Vieja volcano, La Palma Island (Spain), Science of The Total
735   Environment, 843, 157 092, https://doi.org/10.1016/j.scitotenv.2022.157092, 2022.

Rose, W. I. and Durant, A. J.: Fate of volcanic ash: Aggregation and fallout, Geology, 39, 895–896, https://doi.org/10.1130/focus092011.1,
2011.

Ross, P.-S., Dürig, T., Comida, P. P., Lefebvre, N., White, J., Andronico, D., Thivet, S., Eychenne, J., and Gurioli, L.: Standardized analysis
of juvenile pyroclasts in comparative studies of primary magma fragmentation; 1. Overview and workflow, Bulletin of Volcanology, 84,
740   https://doi.org/10.1007/s00445-021-01516-6, 2022.

Rossi, E., Bagheri, G., Beckett, F., and Bonadonna, C.: The fate of volcanic ash: premature or delayed sedimentation?, Nature Communications, 12, 1303, https://doi.org/10.1038/s41467-021-21568-8, 2021.

Rüdiger, J., Tirpitz, L., de Moor, J. M., Bobrowski, N., Gutmann, A., Liuzzo, M., Ibarra, M., and Hoffmann, T.: Multicopter measurements of volcanic gas emissions at Masaya (Nicaragua), Turrialba (Costa Rica) and Stromboli (Italy) volcanoes: Applications for volcano monitoring and insights into halogen speciation, Atmos. Meas. Tech. Discuss. doi, 10, 5194, https://www.academia.edu/download/77757194/e958e61fe2259c91c0602283d9e1bf9f5170.pdf, 2017.

Sasaki, K., Inoue, M., Shimura, T., and Iguchi, M.: In Situ, Rotor-Based Drone Measurement of Wind Vector and Aerosol Concentration in Volcanic Areas, Atmosphere, 12, 376, https://doi.org/10.3390/atmos12030376, 2021.

Schellenberg, B., Richardson, T., Watson, M., Greatwood, C., Clarke, R., Thomas, R., Wood, K., Freer, J., Thomas, H., Liu, E., Salama, F., and Chigna, G.: Remote sensing and identification of volcanic plumes using fixed-wing UAVs over Volcán de Fuego, Guatemala, Journal of Field Robotics, 36, 1192–1211, https://doi.org/10.1002/rob.21896, 2019.

Schmidt, A., Leadbetter, S., Theys, N., Carboni, E., Witham, C. S., Stevenson, J. A., Birch, C. E., Thordarson, T., Turnock, S., Barsotti, S., Delaney, L., Feng, W., Grainger, R. G., Hort, M. C., Höskuldsson, A., Ialongo, I., Ilyinskaya, E., Jóhannsson, T., Kenny, P., Mather, T. A., Richards, N. A. D., and Shepherd, J.: Satellite detection, long-range transport, and air quality impacts of volcanic sulfur dioxide from the 2014–2015 flood lava eruption at Bárdarbunga (Iceland), Journal of Geophysical Research: Atmospheres, 120, 9739–9757, https://doi.org/10.1002/2015JD023638, 2015.

Scollo, S., Coltelli, M., Bonadonna, C., and Del Carlo, P.: Tephra hazard assessment at Mt. Etna (Italy), Natural Hazards and Earth System Sciences, 13, 3221–3233, https://doi.org/10.5194/nhess-13-3221-2013, 2013.

Scollo, S., Prestifilippo, M., Pecora, E., Corradini, S., Merucci, L., Spata, G., and Coltelli, M.: Eruption column height estimation of the 2011-2013 Etna lava fountains, Annals of Geophysics, 57, S0214–S0214, https://doi.org/10.4401/ag-6396, 2014.

Scollo, S., Bonadonna, C., and Manzella, I.: Settling-driven gravitational instabilities associated with volcanic clouds: new insights from experimental investigations, Bulletin of Volcanology, 79, 39, https://doi.org/10.1007/s00445-017-1124-x, 2017.

Scollo, S., Prestifilippo, M., Bonadonna, C., Cioni, R., Corradini, S., Degruyter, W., Rossi, E., Silvestri, M., Biale, E., Carparelli, G., Cassisi, C., Merucci, L., Musacchio, M., and Pecora, E.: Near-Real-Time Tephra Fallout Assessment at Mt. Etna, Italy, Remote Sensing, 11, 2987, https://doi.org/10.3390/rs11242987, 2019.

Shingubara, R., Tsunogai, U., Ito, M., Nakagawa, F., Yoshikawa, S., Utsugi, M., and Yokoo, A.: Development of a drone-borne volcanic plume sampler, Journal of Volcanology and Geothermal Research, 412, 107 197, https://doi.org/10.1016/j.jvolgeores.2021.107197, 2021.

Shinkura, R., Fujiyama, C., and Akiba, S.: Relationship between ambient sulfur dioxide levels and neonatal mortality near the Mt. Sakurajima volcano in Japan, Journal of epidemiology, 9, 344–349, https://www.jstage.jst.go.jp/article/jea1991/9/5/9_5_344/_article/-char/ja/, 1999.

Shinohara, H., Kazahaya, R., Ohminato, T., Kaneko, T., Tsunogai, U., and Morita, M.: Variation of volcanic gas composition at a poorly accessible volcano: Sakurajima, Japan, Journal of Volcanology and Geothermal Research, 407, 107 098, https://doi.org/10.1016/j.jvolgeores.2020.107098, 2020.

Sibaja-Brenes, J. P., Terada, A., Solís, R. A., Luna, M. C., Castro, D. U., Ramírez, D. P., Gutiérrez, R. S., Arroyo, M. M., Godfrey, I., and Cruz, M. M.: Drone monitoring of volcanic lakes in Costa Rica: a new approach, Drone Systems and Applications, 11, 1–14, https://doi.org/10.1139/dsa-2022-0023, 2023.

Simionato, R., Jarvis, P., Rossi, E., and Bonadonna, C.: PlumeTraP: A New MATLAB-Based Algorithm to Detect and Parametrize Volcanic Plumes from Visible-Wavelength Images, Remote Sensing, 14, https://doi.org/10.3390/rs14071766, 2022.

Singh, V.: The Environment and Its Components, in: Textbook of Environment and Ecology, edited by Singh, V., pp. 1–13, Springer Nature, Singapore, ISBN 978-981-9988-46-4, https://doi.org/10.1007/978-981-99-8846-4_1, 2024.

780   Snee, E., Jarvis, P., Simionato, R., Scollo, S., Prestifilippo, M., Degruyter, W., and Bonadonna, C.: Image analysis of volcanic plumes: A simple calibration tool to correct for the effect of wind, Volcanica, 6, 447–458, https://doi.org/10.30909/vol.06.02.447458, 2023.

Sparks, R. S. J.: Forecasting volcanic eruptions, Earth and Planetary Science Letters, 210, 1–15, https://doi.org/10.1016/S0012-821X(03)00124-9, 2003.

Suzuki, Y., Costa, A., Cerminara, M., Esposti Ongaro, T., Herzog, M., Van Eaton, A., and Denby, L.: Inter-comparison
785   of three-dimensional models of volcanic plumes, Journal of Volcanology and Geothermal Research, 326, 26–42, https://doi.org/10.1016/j.jvolgeores.2016.06.011, 2016.

Takishita, K., Poulidis, A.-P., and Iguchi, M.: Tephra segregation profiles based on disdrometer observations and tephra dispersal modeling: Vulcanian eruptions of Sakurajima volcano, Japan, Earth, Planets and Space, 76, 29, https://doi.org/10.1186/s40623-023-01952-y, 2024.

Tang, L. and Shao, G.: Drone remote sensing for forestry research and practices, Journal of Forestry Research, 26, 791–797,
790   https://doi.org/10.1007/s11676-015-0088-y, 2015.

Thivet, S., Gurioli, L., Di Muro, A., Derrien, A., Ferrazzini, V., Gouhier, M., Coppola, D., Galle, B., and Arellano, S.: Evidences of Plug Pressurization Enhancing Magma Fragmentation During the September 2016 Basaltic Eruption at Piton de la Fournaise (La Réunion Island, France), Geochemistry, Geophysics, Geosystems, 21, e2019GC008 611, https://doi.org/10.1029/2019GC008611, 2020a.

Thivet, S., Gurioli, L., Di Muro, A., Eychenne, J., Besson, P., and Nedelec, J.-M.: Variability of ash deposits at Piton de la Four-
795   naise (La Reunion Island): insights into fragmentation processes at basaltic shield volcanoes, Bulletin of Volcanology, 82, 63, https://doi.org/10.1007/s00445-020-01398-0, 2020b.

Thivet, S., Harris, A. J. L., Gurioli, L., Bani, P., Barnie, T., Bombrun, M., and Marchetti, E.: Multi-Parametric Field Experiment Links Explosive Activity and Persistent Degassing at Stromboli, Frontiers in Earth Science, 9, 669 661, https://doi.org/10.3389/feart.2021.669661, 2021.

800   Thivet, S., Carlier, J., Gurioli, L., Di Muro, A., Besson, P., Smietana, M., Boudon, G., Bachèlery, P., Eychenne, J., and Nedelec, J.-M.: Magmatic and phreatomagmatic contributions on the ash-dominated basaltic eruptions: Insights from the April and November–December 2005 paroxysmal events at Karthala volcano, Comoros, Journal of Volcanology and Geothermal Research, 424, 107 500, https://doi.org/10.1016/j.jvolgeores.2022.107500, 2022.

Ventura Diaz, P. and Yoon, S.: High-Fidelity Computational Aerodynamics of Multi-Rotor Unmanned Aerial Vehicles, in: 2018 AIAA
805   Aerospace Sciences Meeting, AIAA SciTech Forum, American Institute of Aeronautics and Astronautics, https://arc.aiaa.org/doi/10.2514/6.2018-1266, 2018.

Vogel, A., Diplas, S., Durant, A. J., Azar, A. S., Sunding, M. F., Rose, W. I., Sytchkova, A., Bonadonna, C., Krüger, K., and Stohl, A.: Reference data set of volcanic ash physicochemical and optical properties, Journal of Geophysical Research: Atmospheres, 122, 9485–9514, https://doi.org/10.1002/2016JD026328, 2017.

810   Watts, A. C., Ambrosia, V. G., and Hinkley, E. A.: Unmanned Aircraft Systems in Remote Sensing and Scientific Research: Classification and Considerations of Use, Remote Sensing, 4, 1671–1692, https://doi.org/10.3390/rs4061671, 2012.

Wilkes, T. C., Pering, T. D., McGonigle, A. J. S., Tamburello, G., and Willmott, J. R.: A Low-Cost Smartphone Sensor-Based UV Camera for Volcanic SO2 Emission Measurements, Remote Sensing, 9, 27, https://doi.org/10.3390/rs9010027, 2017.

Zorn, E. U., Le Corvec, N., Varley, N. R., Salzer, J. T., Walter, T. R., Navarro-Ochoa, C., Vargas-Bracamontes, D. M., Thiele, S. T., and

815   Arámbula Mendoza, R.: Load Stress Controls on Directional Lava Dome Growth at Volcán de Colima, Mexico, Frontiers in Earth Science,

7, https://doi.org/10.3389/feart.2019.00084, 2019.